PAPER

Check for updates

Dinuclear enantiopure Ln³⁺ complexes with (*S*-) and (*R*-) 2-phenylbutyrate ligands. Luminescence, CPL and magnetic properties†

Ànnia Tubau,[a] Francesco Zinna, [ID] [b] Lorenzo Di Bari, [ID] *[b] Mercè Font-Bardía[c] and Ramon Vicente [ID] *[a]

The reaction of $Ln(NO_3)_3 \cdot 6H_2O$ (Ln = Nd, Sm, Eu, Tb, Dy, Tm and Yb) with the respective enantiopure (*R*)-(−)-2-phenylbutyric or (*S*)-(+)-2-phenylbutyric acid (*R/S*-2-HPhBut) and 4,7-diphenyl-1,10-phenanthroline (Bphen) allows the isolation of chiral dinuclear compounds of the formula $[Ln_2(\mu\text{-}R/S\text{-}2\text{-}PhBut)_4(R/S\text{-}2PhBut)_2(Bphen)_2]$ where Ln = Nd³⁺ (*R/S*-**Nd-a**), Sm³⁺ (*R/S*-**Sm-a**), Eu³⁺ (*R/S*-**Eu-a**), Tb³⁺ (*R/S*-**Tb-a** and *R/S*-**Tb-b**), Dy³⁺ (*R/S*-**Dy-a** and *R/S*-**Dy-b**), Tm³⁺ (*R/S*-**Tm-b**) and Yb³⁺ (*R/S*-**Yb-b**). Single crystal X-ray diffraction was performed for compounds **S-Eu-a** and **S-Tm-b**. Powder crystal X-ray diffraction was performed for all complexes. From the crystallographic data two different structural motifs were found which are referred to as structure type *a* and structure type *b*. In structure type *a*, the Ln³⁺ atoms are bridged through four *R* or *S*-2-PhBut ligands with two different kinds of coordination modes whereas in structure type *b* the two Ln³⁺ atoms are bridged through four *R* or *S*-PhBut ligands showing only one kind of coordination mode. For those lanthanide ions exhibiting both structure types, Tb³⁺ and Dy³⁺, a difference in the luminescence and magnetism behavior is observed. All compounds (except *R/S*-**Tm-b**) exhibit sensitized luminescence, notably the Eu³⁺ and Tb³⁺ analogues. Circular Dichroism (CD) and Circular Polarized Luminescence (CPL) in the solid state and in 1 mM dichloromethane (DCM) solutions are reported, leading to improved chiroptical properties for the DCM solutions. The asymmetry factor (g_{lum}) in 1 mM DCM is ±0.02 (+ for *R*-**Eu-a**) for the magnetically allowed transition $^5D_0 \rightarrow {}^7F_1$ and ±0.03 (+ for *R*-**Tb-a** and *R*-**Tb-b**) for the $^5D_4 \rightarrow {}^7F_5$ transition. Magnetic properties of all compounds were studied and the Dy³⁺ compound with the structural motif *b* (*R*-**Dy-b**) shows Single Molecular Magnet (SMM) behavior under a 0 T magnetic field. However, *R*-**Dy-a** is a field-induced SMM.

Introduction

Lanthanide(III) compounds are currently studied mainly for their peculiar magnetic and luminescence properties derived from their partially filled 4f valence shell. Regarding magnetic properties, since the discovery of the first mononuclear lanthanide complexes of formula $[Pc_2Ln]^- \cdot TBA^+$ (Ln = Tb³⁺, Dy³⁺; Pc = dianion of phthalocyanine; TBA⁺ = tetrabutylammonium)

[a]Departament de Química Inorgànica i Orgànica, Secció de Química Inorgànica, Universitat de Barcelona, Martí i Franquès 1-11, 08028 Barcelona, Spain. E-mail: rvicente@ub.edu
[b]Dipartimento di Chimica e Chimica Industriale, Università di Pisa, via Moruzzi 13, I 56124 Pisa, Italy. E-mail: lorenzo.dibari@unipi.it
[c]Departament de Mineralogia, Cristal·lografia i Dipòsits Minerals i Unitat de Difracció de Raigs X, Centres Científics i Tecnològics de la Universitat de Barcelona (CCiTUB), Universitat de Barcelona, Solé i Sabarís 1-3, 08028 Barcelona, Spain
†Electronic supplementary information (ESI) available: Tables S1–S7 and Fig. S1–S17. See DOI: https://doi.org/10.1039/d4dt01295j

showing slow relaxation of the magnetization and acting as single-molecule magnets (SMMs),[1] a plethora of mono and polynuclear SMM complexes derived from lanthanide ions with large orbital momentum and strong magnetic anisotropy have been reported.[2] On the other hand, lanthanide(III) complexes with luminescence properties are of interest due to their applications in materials and biosciences.[3] The preparation of chiral lanthanide(III) coordination compounds is of high current interest to achieve circularly polarized luminescence (CPL)[4] for applications in circularly polarized organic light-emitting diodes (CP-OLEDs),[5] biological sensing[6] and anti-counterfeiting devices.[7] Moreover, CPL active lanthanide complexes are studied in the context of molecular magnetism.[8]

Chiral ligands naturally induce a dissymmetric environment around the Ln³⁺ ion, which determines the onset of chiroptical properties allied to the f–f transitions of the ion. In emission, this is sensitively monitored through CPL, which

can be conveniently quantified by means of the dissymmetry factor g_{lum}, eqn (1):

$$g_{lum} = 2\frac{I_L - I_R}{I_L + I_R} = 2\frac{\Delta I}{I} \qquad (1)$$

where I_L and I_R are the left and right circularly polarized components of the emission of the compound.

Usually, non-aggregated organic molecules or d-metal complexes, with a few exceptions particularly concerning chromium(III),[9a–e] display g_{lum} factors of the order of 10^{-4}–10^{-3},[9f–h] while lanthanide complexes may show much higher values (10^{-1}–1.4).[10] Usually, CPL is measured for mononuclear Eu^{3+} complexes, while it is more rarely investigated for complexes with higher nuclearity, such as binuclear helicates[11] or trinuclear[12] and heptanuclear[13] systems.

In previously published papers, we have used the chiral bidentate bridging carboxylate ligands generated from (S)-(+)- or (R)-(−)-2-phenylpropionic acid and S-(+)- and R-(−)-2-(6-methoxy-2-naphthyl)propionic acid to synthesize two series of enantiomeric pure dinuclear 4f-metal ion complexes of the formula $[Ln_2(S\text{-}L)_6(phen)_2]$ or $[Ln_2(R\text{-}L)_6(phen)_2]$ (HL = chiral carboxylic acid) by adding simultaneously neutral chelating 1,10-phenanthroline (phen) ligands which block two coordination sites per Ln^{3+} ion and terminate further aggregation.[14] The 1,10-phenanthroline ligands also have a role of sensitizing the luminescence of the lanthanide ion, through the so-called antenna effect. In fact, because of the weak f–f absorption of Ln^{3+} ions, a suitable chromophore organic ligand should be employed to populate the lanthanide emitting states through an energy transfer process.[15]

We have also recently published a series of 1D coordination compounds with the formula $[Ln(\mu\text{-}R\text{-}MPA)(R\text{-}MPA)_2(phen)]_n$ or $[Ln(\mu\text{-}S\text{-}MPA)(S\text{-}MPA)_2(phen)]_n$ for R- or S-HMPA, respectively (Ln = Eu, Tb, Dy and Sm) where R- or S-MPA is the anionic salt of the R- or S-α-methoxyphenylacetic acid.[16]

With the aim of obtaining new lanthanide compounds in which luminescence, chiroptical and magnetic properties could coexist, and therefore obtaining multifunctional materials, we present herein the structural, magnetic and optical studies of a new series of chiral lanthanide coordination complexes derived from the enantiomeric pure R- or S-2-phenylbutyric acid (R/S-2-HPhBut), Scheme 1(a), and the auxiliary ligand 4,7-diphenyl-1,10-phenanthroline (Bphen), Scheme 1(b). The reaction of the above ligands with the respective nitrate lanthanide salts leads to new dinuclear com-

plexes with the formula $[Ln_2(\mu\text{-}R/S\text{-}2\text{-}PhBut)_4(R/S\text{-}2PhBut)_2(Bphen)_2]$ showing two different structural motifs *a* and *b* with coordination numbers 9 and 8 respectively, where Ln = Nd^{3+} (R/S-**Nd-a**), Sm^{3+} (R/S-**Sm-a**), Eu^{3+} (R/S-**Eu-a**), Tb^{3+} (R/S-**Tb-a** and R/S-**Tb-b**), Dy^{3+} (R/S-**Dy-a** and R/S-**Dy-b**), Tm^{3+} (R/S-**Tm-b**) and Yb^{3+} (R/S-**Yb-b**). Luminescence as well as Circular Dichroism (CD) and Circular Polarized Luminescence (CPL) measurements were performed in solid and in 1 mM DCM solutions. Also, the static and dynamic magnetic studies of the presented complexes are discussed in this work. In a remarkable way, the Dy^{3+} compound with the structural motif *b* (***R*-Dy-b**) shows Single Molecular Magnet (SMM) behavior under a 0 T magnetic field. However, ***R*-Dy-a** is a field-induced SMM. Moreover, ***R*-Nd-a** and ***R*-Yb-b** are also field-induced SMMs.

Experimental section

Starting materials

(R)-(−)-2-Phenylbutyric acid (R-2-HPhBut), (S)-(+)-2-phenylbutyric acid (S-2-HPhBut) and bathophenanthroline (Bphen) were purchased from Sigma-Aldrich. The $Ln(NO_3)_3 \cdot 6H_2O$ salts were obtained from Strem Chemicals. All the reactants were used as received.

## Syntheses of $[Ln_2(\mu\text{-}R/S\text{-}2PhBut)_4(R/S\text{-}2PhBut)_4(Bphen)_2]$

Into 20 mL of an ethanolic solution‡ in a 1:1 ratio, the respective R or S-(− or +)-2-phenylbutyric acid (1.5 mmol, 246.3 mg) and KOH (1.5 mmol, 84.2 mg) were dissolved. Separately, a DMF solution containing 4,7-diphenyl-1,10-phenanthroline (Bphen) (0.5 mmol, 166 mg) was heated until it had dissolved (around 55 °C). Then the amine solution was added to the previous ethanolic solution. The resulting solution was stirred for 10 min. Afterwards, a DMF solution containing the respective $Ln(NO_3)_3 \cdot 6H_2O$ salt (0.5 mmol) was added. The light pink transparent solution was magnetically stirred for 15 minutes at 55 °C. Then the reaction solution was cooled down to room temperature and left to stand to crystallize through slow evaporation. White crystals appear after two weeks. Crystals obtained in the synthesis were dissolved in 3 mL of DMF and the solutions were left to crystallize through slow vapor diffusion with acetonitrile to obtain suitable crystals for the single crystal X-ray diffraction measurement of ***S*-Eu-a** and ***S*-Tm-b**.

Selected IR-ATR bands as well as elemental analyses of compounds ***R/S*-Nd-a** to ***R/S*-Yb-b** are compiled in the ESI.†

IR and magnetic measurements

Infrared spectra (4000–400 cm^{-1}) were recorded from KBr pellets on a Perkin-Elmer 380-B spectrophotometer. Magnetic measurements were performed using a Mesures Magnètiques Unit from Scientific and Technological Centers (CCiTUB),
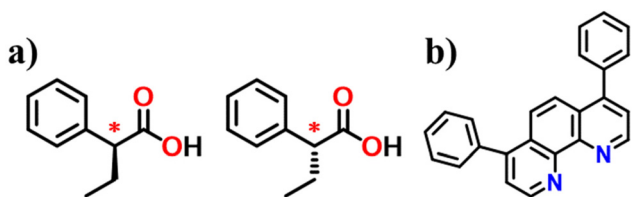
Scheme 1 (a) R/S-(−/+)-2-Phenylbutanoic acid (R/S-2-HPhBut) (b) bathophenanthroline (Bphen).

‡To obtain structure *a* of the $[Tb_2(\mu\text{-}2\text{-}R/S\text{-}PhBut)_4(R/S\text{-}2PhBut)_4(Bphen)_2]$ compound, the solvent used in this step should be methanol instead of ethanol.

Universitat de Barcelona, using a Quantum Design MPMS-XL SQUID magnetometer. Pascal's constants were used to estimate the diamagnetic corrections, which were subtracted from the experimental susceptibilities to give the corrected molar magnetic susceptibilities.

Luminescence properties

Solid-state fluorescence spectra of the compounds were recorded on a Horiba Jobin Yvon SPEX Nanolog fluorescence spectrophotometer (Fluorolog-3 v3.2, HORIBA Jobin Yvon, Cedex, France) equipped with a three-slit double grating excitation and emission monochromator with dispersions of 2.1 nm mm^{-1} (1200 grooves per mm) at room temperature. The steady-state luminescence was excited using unpolarized light from a 450 W xenon CW lamp and detected using a red-sensitive Hamamatsu R928 photomultiplier tube at an angle of 22.5° for solid-state measurements and at an angle of 90° for solution measurements. The equipment was adjusted to obtain the highest background-to-noise ratio. Spectra were corrected for both the excitation source light intensity variation (lamp and grating) and the emission spectral response (detector and grating). Near infra-red spectra were recorded at an angle of 22° using a liquid nitrogen-cooled, solid indium/gallium/arsenic detector (850–1600 nm). To measure the emission spectra, solid-state samples were excited at excitation wavelengths (λ_{exc}) of 355, 354, 360, 360, 355, 355, 356 and 359 nm for **S-Sm-a**, **S-Eu-a**, **S-Dy-a**, **S-Dy-b**, **S-Tb-a**, **S-Tb-b**, **S-Nd-a** and **S-Yb-b** respectively. Emission spectra of the DCM solutions were monitored at a λ_{exc} of 284 nm for all compounds.

The photoluminescence time decay curves were measured with the same instrument in the phosphorescence mode using a 450 W xenon pulsed lamp (1.5 ns pulse). The experiments were monitored at the respective λ_{exc} and emission wavelength (λ_{em}) of 615 nm ($^5D_0 \rightarrow {}^7F_2$) for **S-Eu-a** and 546 nm ($^5D_4 \rightarrow {}^7F_5$) for **S-Tb-a** and **S-Tb-b**.

The measured decays were analyzed using the Origin software package. Both decay curves were fitted monoexponentially: $I(t) = I_0 \exp\left(-\dfrac{t}{t_{obs}}\right)$. The fit quality was determined using the χ^2 method of Pearson. Luminescence quantum yields (ϕ_{Ln}^L) were recorded using an absolute PL quantum yield spectrometer from Hamamatsu Photonics upon excitation of the samples at the respective λ_{exc}.

Chiroptical spectroscopy measurements

ECD spectra. The ECD spectra were recorded with a Jasco J-1500 spectropolarimeter on polycrystalline samples dispersed in a KBr matrix. In order to check for and minimize the contributions from linear dichroism/linear birefringence, for each sample, different spectra were recorded rotating the sample by 180° around the optical axis and then all the spectra were averaged. Solution spectra were recorded in DCM solution (1 mM) in a 1 cm cell.

CPL spectra. The circularly polarized luminescence experiments for compounds **S/R-Eu-a** and **S/R-Tb-b** were carried out with a home-built CPL spectrofluoropolarimeter[17] that acquired simultaneously the luminescence and CPL data, under UV irradiation (λ_{max} = 254 nm) on quartz plate depositions and on 1 mM DCM solutions. The depositions of the complexes were obtained from *n*-pentane dispersions. *n*-Pentane was chosen as a dispersant as it does not dissolve the compounds and in this way the complexes are deposited as a microcrystalline powder film. The spectra were acquired rotating the sample by ±90° around the optical axis and by flipping the sample by 180° around the axis perpendicular to the collection beam. At least 2 spectra were recorded for each configuration. All the spectra were then averaged to give the final spectra. Acquisition parameters: slit width 0.5 mm, scan speed 0.5 nm s^{-1}, integration time 2 s, PMT voltage 680/700 V.

X-ray crystallography. Good quality crystals of **S-Eu-a** and **S-Tm-b** were selected and mounted on a D8VENTURE (Bruker) diffractometer with a CMOS detector. The crystallographic data, conditions retained for the intensity data collection, and some features of the structure refinements are listed in Table S1.† All the structures were refined using the least-squares method. Intensities were collected with multilayer monochromated Mo-Kα radiation. Lorentz polarization and absorption corrections were made for the **S-Eu-a** and **S-Tm-b** crystal measurements. The structures were solved by direct methods, using the SHELXS-97 computer program[18] and refined using the full-matrix least-squares method, using the SHELXL-2014 computer program.[19] The non-hydrogen atoms were located in successive difference Fourier syntheses and refined with anisotropic thermal parameters on F^2. For hydrogen atoms, isotropic temperature factors were assigned to be 1.2 irrespective of the C atom to which the H was attached.

Results and discussion

Structural characterization of R/S-[Ln$_2$(μ-2-PhBut)$_4$(2-PhBut)$_2$(Bphen)$_2$]

Single crystal X-ray diffraction measurements were performed for compounds **S-Eu-a** and **S-Tm-b**. Selected bond distances of **S-Eu-a** and **S-Tm-b** and crystallographic information are listed in Tables S1 and S2† respectively. Partially labelled plots of the structure of compounds **S-Eu-a** and **S-Tm-b** are shown in Fig. 1, top.

All the synthesized compounds have the same molecular formula, but from the crystallographic data two different structural motifs can be found, structure type a (*structure a*) and structure type b (*structure b*). *Structure a* is found in the **S-Eu-a** compound, which crystallizes in a triclinic crystal system in the $P1$ space group.

Each asymmetric unit is constituted by a dinuclear entity in which each Eu^{3+} is nonacoordinated. In each dinuclear unit, the two Eu^{3+} atoms are bridged by four (S)-(+)-2-phenylbutirate ligands (S-2-PhBut) through two different coordination modes. Two of the bridging S-2-PhBut ligands are in the symmetrical *syn–syn* bidentate bridging coordination mode ($\eta_1:\eta_1:\mu_2$ or 2.11 using Harris notation[20]) (Scheme 2a) with Eu–O bond lengths
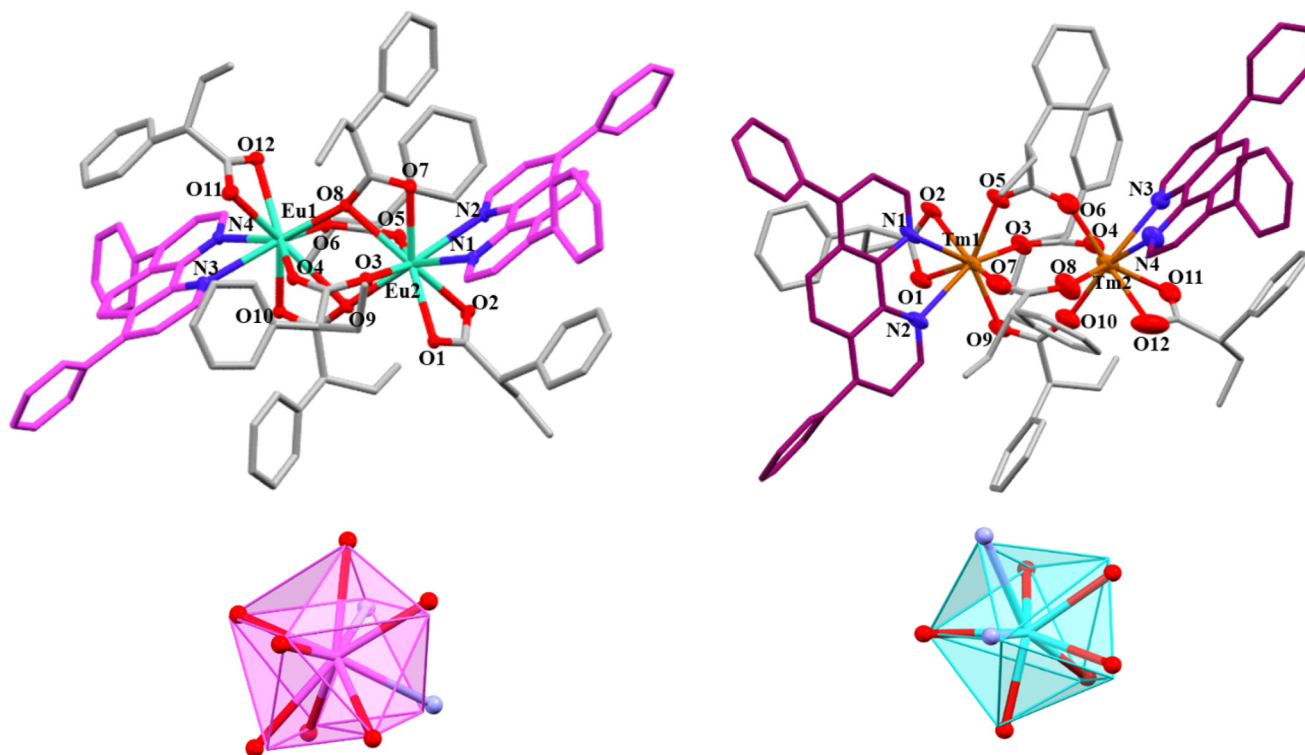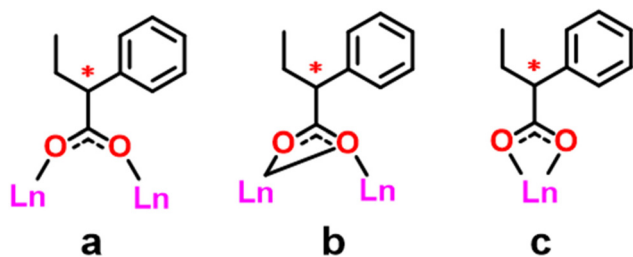
Fig. 1 Top, partially labeled plots of compounds *S*-Eu-a (left) and *S*-Tm-b (right). H atoms have been omitted for a better view of the structure. Bottom, idealized coordination polyhedron compared with the real positions of the coordinating atoms of *S*-Eu-a (pink) and *S*-Tm-b (blue).

Scheme 2 Coordination modes of *S/R*-2-PhBut. (a) Symmetrical *syn–syn* bidentate bridging, (b) chelating-bridging and (c) chelating coordination mode.

ranging between 2.356(5) and 2.413(4) Å. The other two *S*-2-PhBut bridging ligands are best described as chelating-bridging (η_1:η_2:μ_2 or 2.21) (Scheme 2b) in which O8 and O9 connect the two Eu atoms with bond distances in the 2.326(4)–2.773(4) Å range; meanwhile O7 and O10 are bonded only to a Eu atom with Eu–O bond lengths of 2.518(5) and 2.401(5) Å respectively. The Eu1···Eu2 intramolecular distance is 4.000(5) Å. Moreover, there are two *S*-2-PhBut ligands coordinated to each Eu center in the monodentate chelating coordination mode (Scheme 2c) with Eu–O bond distances in the 2.404(4)– 2.543(4) Å range. Finally, each EuN_2O_7 coordination sphere is completed by two N atoms from the bathophenanthroline ligand (Bphen) with Eu–N distances in the 2.567(4)–2.649(4) Å range. To determine the distortion degree of each lanthanide

ion coordination polyhedron the SHAPE software[21] was used. The distortion degree was quantified as Continuous Shape Measurement (CShM) values. For the former compound, the coordination polyhedron is close to a Muffin geometry (MFF-9, Cs) with a CShM value of 1.616 for both Eu^{3+} centers, as shown in Fig. 1, bottom. The europium ions of each dinuclear entity are crystallographically independent, but both have the same coordination environment. The molecules are arranged in space through π–H stacking from the Bphen ligands. Centroid 1 (Cg1), formed by C97, C98, C99, C107, C108 and C109, interacts with H24 bonded to an sp^2 carbon (C24) from one aromatic ring of the Bphen ligand of the adjacent dinuclear unit, with a Cg1···H24 intramolecular distance of 2.540 Å, Fig. 2. The π–H stacking interaction grows along the [0 0 1] space vector.

On the other hand, the structure type *b* is found in *S*-Tm-b. It crystallizes in the monoclinic crystal system and the *C*2 space group. The asymmetric unit of *S*-Tm-b is composed of a dinuclear system where each Tm^{3+} ion is octacoordinated. The thulium centers are bridged through four carboxylate *S*-2-PhBut ligands that are in the symmetrical *syn–syn* bidentate bridging coordination mode with Tm–O distances ranging from 2.234(9) to 2.291(7) Å. The intramolecular distance between the two Tm metals is 4.287(7) Å. Also, there are two *S*-2-PhBut ligands, coordinated one to each lanthanide center, in the monodentate chelating coordination mode and Tm–O distances in the 2.312(9)–2.412(8) Å range. Each TmN_2O_6 coordination sphere is fulfilled by two N atoms from one Bphen
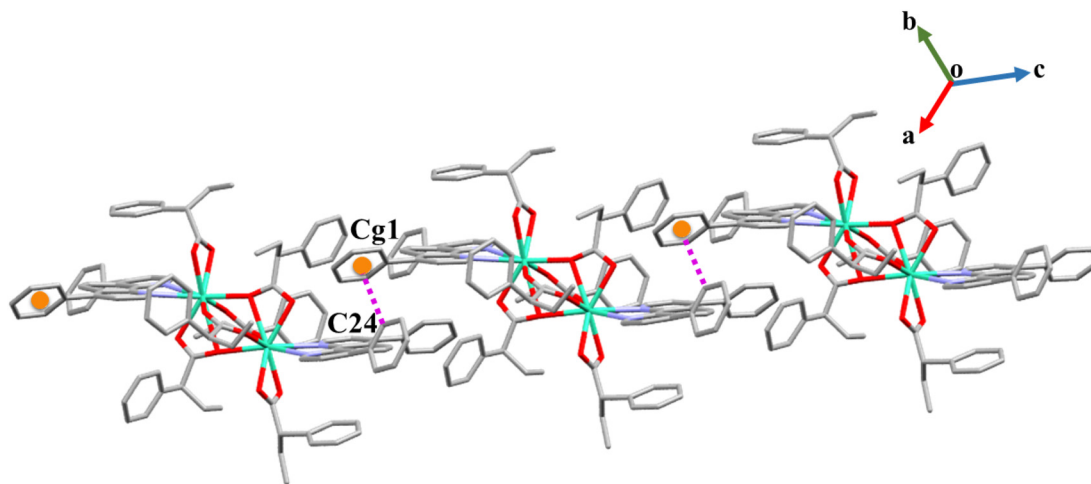
Fig. 2 π–H stacking intramolecular interactions along the **S-Eu-a** crystal lattice. The orange balls represent the calculated centroid of the Bphen aromatic rings. The π–H stacking interaction is represented by the pink dotted lines.

ligand with Tm–N distances in the 2.516–2.585 Å range. The coordinating N and O atoms are set around each Tm^{3+} ion in a geometry close to a triangular dodecahedron (TDD-8, D_2d) with a CShM value of 1.288. Each Tm center of the same dinuclear unit is crystallographically independent but both are placed in the same environment inside the lattice. Moreover, there are no π–H or π–π interactions with distances short enough to consider stacking between the dinuclear molecules in **S-Tm-b**.

The main difference between the structural motifs *a* or *b* is the coordination mode of the bridging ligands, Scheme 3. In *structure b*, the four of them are found in the same *syn–syn* bidentate bridging mode while in *structure a*, besides the two carboxylate ligands in the *syn–syn* bidentate bridging mode, the other two *S/R*-2-PhBut bridging ligands are found in the chelating-bridging coordination mode. Consequently, the coordination number decreases from 9, in *structure a*, to 8, in *structure b*. The distinction in the coordination number leads the chelating *S*-2-PhBut and Bphen ligands to rearrange differ-

ently in space also, changing the geometry of the coordination polyhedron from the crystal motif *a* to *b*.
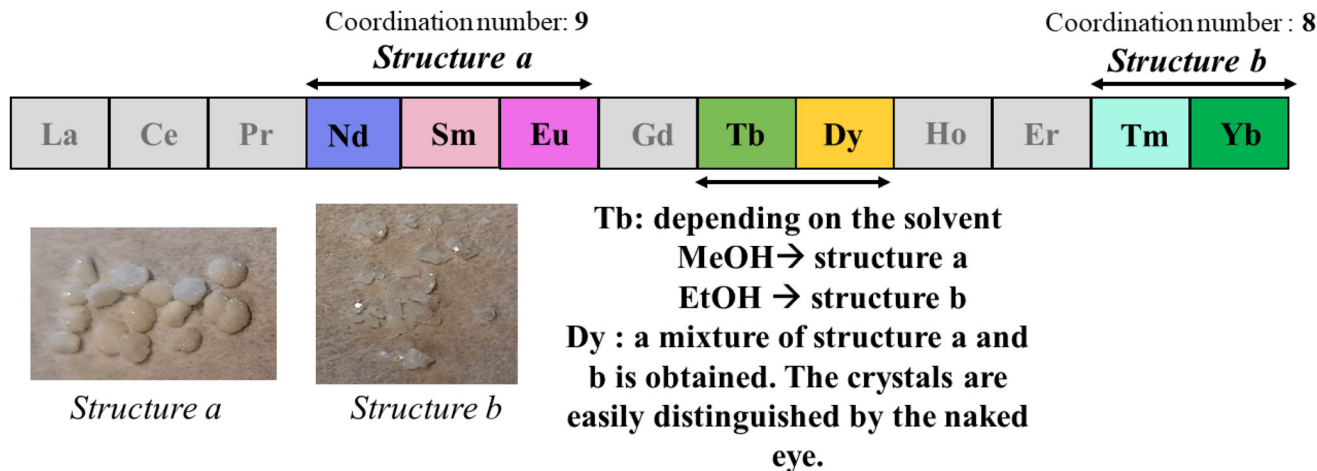
Moreover, the Powder X-Ray Diffraction (PXRD) of **S-Eu-a** and **S-Tm-b** samples matched well with the calculated PXRD patterns obtained from the single crystal structure, confirming its phase purity, Fig. S1.†

Then enantiopure compounds **R-Eu-a** and **R-Tm-b**, as well as both the enantiomeric pairs, were synthesized using other lanthanide ions such as Nd^{3+}, Sm^{3+}, Tb^{3+}, Dy^{3+} and Yb^{3+}. PDRX was performed for all the analogues (Fig. S2 and S3†). Interestingly, different diffractograms corresponding to structure *a* and structure *b* were obtained depending on the lanthanide ion. The trend goes as follows (Scheme 4): (i) for Nd^{3+}, Sm^{3+} and Eu^{3+}, the final product crystallizes as *structure a* (**S/R-Nd-a**, **S/R-Sm-a** and **S/R-Eu-a**) whereas (ii) for Tm^{3+} and Yb^{3+}, the final product crystallizes as *structure b* (**S/R-Tm-b** and **S/R-Yb-b**). (iii) Meanwhile, for Tb^{3+} and Dy^{3+} ions, both structure types are obtained. For Tb^{3+} the final structural motif depends on the solvent used during the reaction. In a methanol/DMF
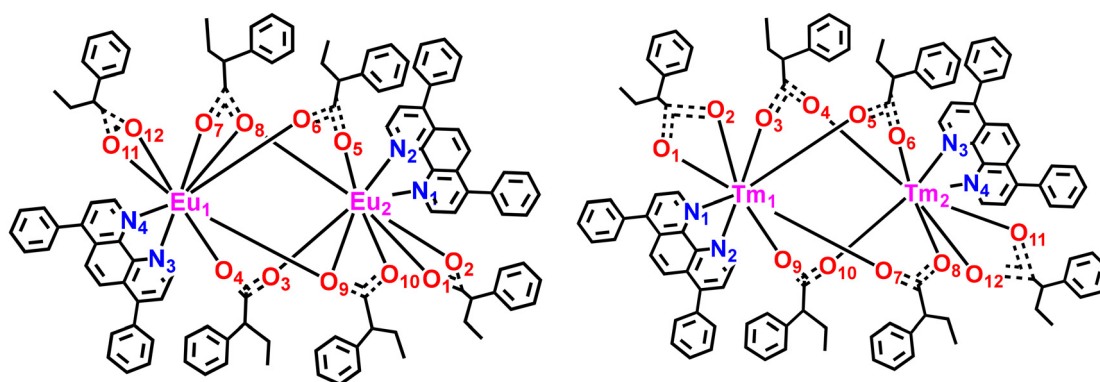
Scheme 3 Scheme of structure type a (left) and structure type b (right). The atoms are numbered as in the structures of compounds **S-Eu-a** and **S-Tm-b** which show the structural motifs *a* and *b*, respectively.

Coordination number: **9**   Coordination number : **8**
Structure a   *Structure b*

| La | Ce | Pr | **Nd** | **Sm** | **Eu** | Gd | **Tb** | **Dy** | Ho | Er | **Tm** | **Yb** |

Structure a   *Structure b*

**Tb: depending on the solvent
MeOH→ structure a
EtOH → structure b
Dy : a mixture of structure a and
b is obtained. The crystals are
easily distinguished by the naked
eye.**

Scheme 4 Structural trend along the lanthanide group.

solution, a Tb^{3+} compound with the *structure a* (*S/R*-**Tb-a**) type is obtained. If ethanol instead of methanol is used, the Tb^{3+} final compound shows the *structure b* (*S/R*-**Tb-b**) type. For the Dy^{3+} analogue, a mixture of both structures is obtained. Since the crystals corresponding to *structure a* and *structure b* can be discerned by the naked eye, each structure type can be isolated for *S* and *R*-Dy compound (*S/R*-**Dy-a** and *S/R*-**Dy-b**).

The trend observed for the presented *R/S*-[Ln₂(μ-2-PhBut)₄(2-PhBut)₂(Bphen)₂] lanthanide family is mainly due to the gradual decrease in the lanthanide(III) ionic radius on increasing the atomic number, the so-called lanthanide contraction.[3a,22] The reduction of the Ln^{3+} radii induces a decrease in the coordination number which implies a change in the final structure. As the Ln^{3+} radius decreases, the coordination number diminishes from 9 (*structure a*), for the lighter lanthanides, to 8 (*structure b*) for the heaviest ones. The lanthanide elements located in the middle of the period show both coordination numbers as *structure a* and *structure b*. For the Tb^{3+} analogue, the obtaining of one structural type or the other is discriminated by the solvent used in each synthesis.

In addition, the contraction along the lanthanide series is also observed in the Ln–O and Ln–N bond distances in the *S*-**Eu-a** and *S*-**Tm-b** structures. The overall Eu–O and Eu–N bond lengths are larger than those for Tm–O and Tm–N. The Ln···Ln intermolecular distance, though, is larger for *S*-**Tm-b** (4.287 Å) compared to *S*-**Eu-a** (4.000 Å). This is because in *S*-**Eu-a**, the Eu^{3+} ions are bridged, apart from the bridging ligand, through one oxygen atom from each chelating-bridging carboxylate ligand which generates an Ln–O–Ln angle, shortening in this way the Eu···Eu intramolecular distance.

Luminescence properties

The luminescence properties of all compounds were measured in the solid state and in 1 mM dichloromethane (DCM) solution at room temperature. Since each enantiomer pair shows the same luminescence properties, only the *S*-enantiomer of each lanthanide is discussed in this section. The excitation spectra of the polycrystalline enantiomers were recorded at the emission wavelength (λ_{em}) of 1062 nm ($^4F_{3/2} \rightarrow {}^4I_{11/2}$) for *S*-**Nd-a**, at 597 nm ($^4G_{5/2} \rightarrow {}^6H_{9/2}$) for *S*-**Sm-a**, at 615 nm ($^5D_0 \rightarrow {}^7F_2$) for *S*-**Eu-a**, at 546 nm ($^5D_4 \rightarrow {}^7F_5$) for *S*-**Tb-a** and *S*-**Tb-b**, at 574 nm for *S*-**Dy-a**, at 576 nm ($^4F_{9/2} \rightarrow {}^6H_{13/2}$) for *S*-**Dy-b** and at 975 nm ($^2F_{5/2} \rightarrow {}^2F_{7/2}$) for *S*-**Yb-b** (Fig. S4†). All the spectra show an intense and broad band around 300–400 nm that is assigned to the $\pi \rightarrow \pi^\star$ and $n \rightarrow \pi^\star$ excitation transitions from the Bphen ligand. In addition, for compound *S*-**Sm-a**, a weak band appears at around 403 nm and it is assigned to the intrinsic $^6H_{5/2} \rightarrow {}^4F_{7/2}$ f–f transition. The shoulder found in the 375–400 nm range in the *S*-**Dy-a** and *S*-**Dy-b** spectra could be attributed to the $^6H_{15/2} \rightarrow {}^6P_{7/2}$ and $^6H_{15/2} \rightarrow {}^6P_{5/2}$ centered f–f excitation transitions.[23] Absorption spectra were recorded for all complexes, the free Bphen ligand ($c = 1$ mM) and deprotonated *S*-2-PhBut DCM solutions, as shown Fig. S5;† the latter was recorded in the presence of KOH. All spectra show similar absorption patterns. The maximum appearing at 284 nm is assigned to the $\pi \rightarrow \pi^\star$ and $n \rightarrow \pi^\star$ transitions in the Bphen ligand. In the superimposed spectra of the Bphen free ligand, the maximum is slightly blue shifted in comparison with the *S*-**Eu-a** spectrum indicating coordination to the metal.

Emission spectra were monitored by exciting the samples at their respective absorption maxima, in the solid and DCM phases. This resulted in the emission of the predicted lanthanide f–f transitions within the visible and NIR ranges. Besides, the characteristic red and green luminescence colour of Eu and Tb-based systems could be seen by the naked eye. For a more accurate comparison of their luminescence, emission spectra of *S*-**Tb-a**/*S*-**Tb-b** and *S*-**Dy-a**/*S*-**Dy-b** pairs were monitored under the exact same conditions. The expected profiles were recorded in all cases, with some differences in the polycrystalline and solution samples, except for *S*-**Dy-a** and *S*-**Dy-b**, where no significant emission was observed in solution. The luminescence properties of *S*-**Tm-b** are not discussed as its
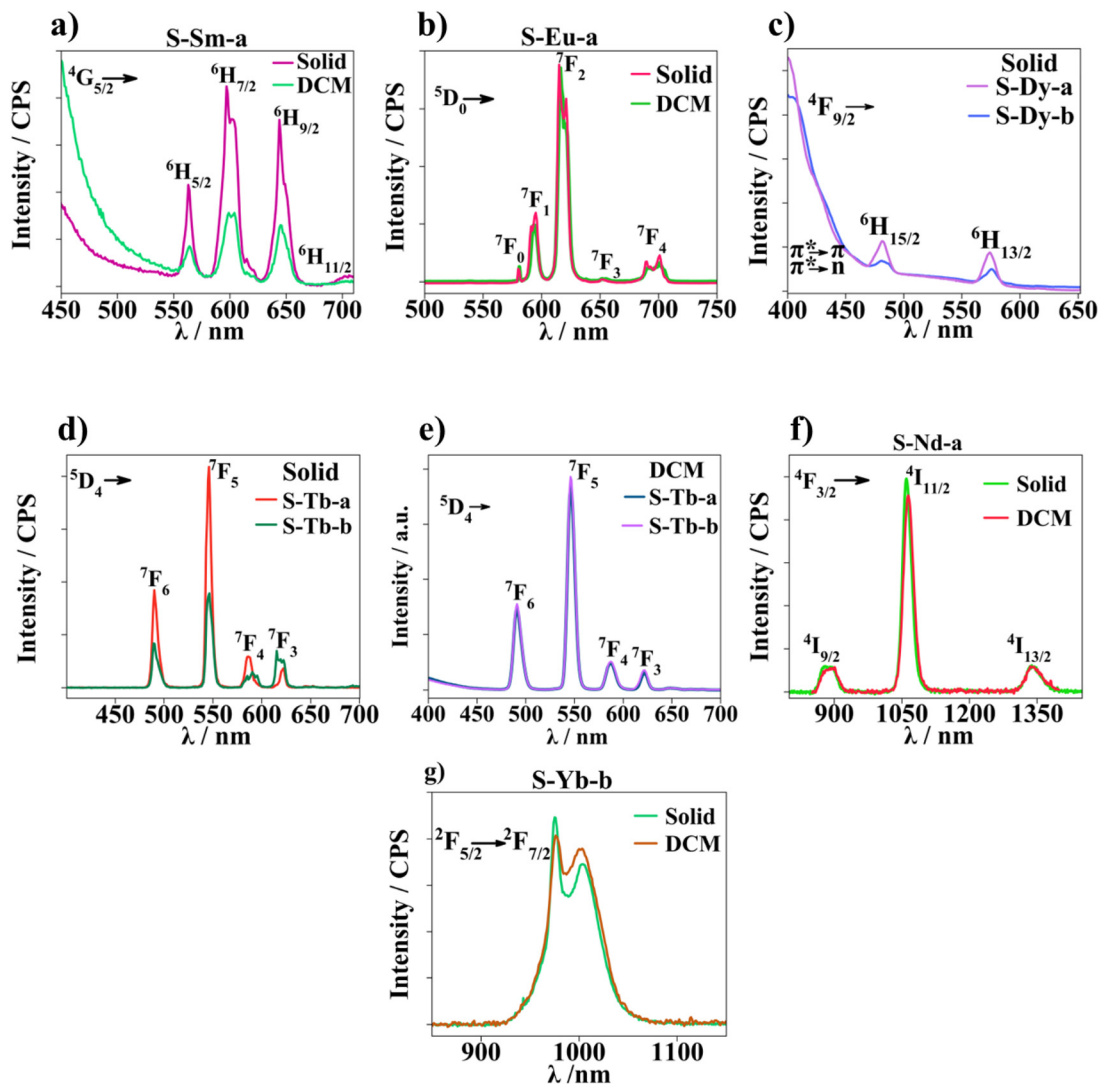
Fig. 3 Emission spectra of all compounds measured in the solid state and in 1 mM DCM solution.

emission spectrum is entirely dominated by ligand emission. Emission bands exhibited by the former lanthanide complexes are presented in Fig. 3 and a compilation of the wavelengths assigned to each transition can be found in Table S3.†

Excitation of **S-Sm-a** led to emission bands at 563, 597, and 644 and a weak one at 705 nm, Fig. 3(a). The bands are assigned to the transitions from the $^4G_{5/2}$ emitting level to the ^6H_J level where J is 5/2, 7/2, 9/2 and 11/2, respectively. Residual emission from the ligand, which becomes more prominent in DCM solution, is detected at 450–500 nm indicating a rather low sensitization efficiency for **S-Sm-a**.

The expected Eu^{3+} bands corresponding to the $^5D_0 \rightarrow {}^7F_{J=0-4}$ transition are distinguished after the excitation of **S-Eu-a**, Fig. 3(b). The forbidden transition ($\Delta J = 0$) appears as a sharp, low-intensity band at 581 nm. For the $^7F_0$ ground state, the splitting due to crystal field perturbation is 1. Hence, any splitting of the emission band associated with the 0 → 0 transition suggests the presence of more than one Eu^{3+} emitting center,

each with a different environment. In the crystal structure of the dinuclear **S-Eu-a** compound, there are two Eu^{3+} ions that are crystallographically independent, although each has the same chemical environment, and both have the same coordination geometry (CShM is the same). Therefore, compound **S-Eu-a** has one Eu^{3+} emitting center with a single 0 → 0 emission band. The magnetically allowed $^5D_0 \rightarrow {}^7F_1$ transition, with intensity independent of the environment, arises at 594 nm and it is split due to the crystal field. The most intense band located in the red range at 615 nm is assigned to the $^5D_0 \rightarrow {}^7F_2$ transition and it is mostly responsible for the red emission colour of **S-Eu-a**. The splitting of the hypersensitive band suggests that the lanthanide ion does not occupy an inversion symmetry site inside the structure found in solid and in solution samples. Finally, the broader band at 701 nm which is also split due to crystal field perturbation is assigned to the $^5D_0 \rightarrow {}^7F_4$ transition.[24] Polycrystalline and DCM spectra of **S-Eu-a** appear to be rather similar; however on dissolving the

solid sample into the 1 mM DCM solution, splitting of $^5D_0 \rightarrow {}^7F_1$ due to crystal field perturbation is not seen anymore, indicating some sort of structural change in solution, Fig. S6.†

S-Tb-a and **S-Tb-b** polycrystalline powders show the bands arising from f–f Tb^{3+} transitions at 491, 546, 585 and 623 nm which are assigned to $^5D_4 \rightarrow {}^7F_{J=6-3}$. The **S-Tb-a** signals are more intense than the ones corresponding to the **S-Tb-b** isomer, as also seen for the measured quantum yields (see below). Besides, for **S-Tb-b**, the bands corresponding to $^5D_4 \rightarrow {}^7F_4$ and $^5D_4 \rightarrow {}^7F_3$ transitions are split due to crystal field perturbation. Furthermore, the spectra of both **S-Tb-a** and **S-Tb-b** show the same pattern when they are found in DCM solution (Fig. 3e) and at the same time the two spectra are different from the polycrystalline sample suggesting that the dinuclear unit is probably not maintained when dissolving the **S-Tb-a** and **S-Tb-b** compounds in DCM.

As for the Dy-based systems, when exciting the polycrystalline **S-Dy-a** and **S-Dy-b** samples at the corresponding ligand excitation wavelengths, very weak emission corresponding to the Dy^{3+} luminescence could be measured, Fig. 3c. Weak bands at 481 and 574 nm correspond to the $^7F_{9/2} \rightarrow {}^6H_{15/2}$ and $^7F_{9/2} \rightarrow {}^6H_{13/2}$ transitions; however, the emission spectra are mainly governed by a more intense and broader band in the blue range (400–450 nm) corresponding to ligand emission. For **S-Dy-a** and **S-Dy-b** in DCM solution, the luminescence is totally quenched, and just emission from the ligand can be detected (spectra not shown).

Regarding the NIR emitters, after exciting the **S-Nd-a** powder at the ligand wavelength, emission from the Nd^{3+} ion is clearly recognized, as shown in Fig. 3f. The more intense band arising at 1061 nm is assigned to $^4F_{3/2} \rightarrow {}^4I_{11/2}$ whereas the two less intense bands at 886 and 1339 nm correspond to $^4F_{3/2} \rightarrow {}^4I_{9/2}$ and $^4F_{3/2} \rightarrow {}^4I_{13/2}$ transitions.

Finally, the expected luminescence band from the Yb^{3+} ion is induced after the excitation of **S-Yb-b**. The band appearing at 976 nm corresponds to the $^2F_{5/2} \rightarrow {}^2F_{7/2}$ transition and is split due to crystal field perturbation.[3a,25]

The emission spectra in solution are slightly different compared to the polycrystalline spectra. This may indicate a change in the lanthanide coordination environment due to solvation effects or due to the stability of the compounds in solution.

For instance, thanks to europium's pure magnetic dipole and electric dipole nature of the $^5D_0 \rightarrow {}^7F_1$ and $^5D_0 \rightarrow {}^7F_2$ transitions respectively, some structural information can be obtained from its luminescence spectra. The integrated area of the $^5D_0 \rightarrow {}^7F_1$ band to the area of the $^5D_0 \rightarrow {}^7F_2$ band ratio (0 → 1/0 → 2) provides information about the symmetry around the Eu^{3+} environment.[24] For the polycrystalline sample the ratio value is 0.3 while in solution it changes to 0.2 indicating that a slight change is produced around the Eu^{3+} site on dissolving the sample in DCM solution. Furthermore, spectra of both **S-Tb-a** and **S-Tb-b** are comparable when they are found in DCM solution, as already mentioned, suggesting that the dinuclear unit is not maintained. Instead, a new compound, probably a mononuclear system, is found and perhaps an equi-

librium of different species is active in solutions. Because good luminescence properties are retained in the solution samples, the solvated systems could correspond to a molecular system where the **S-PhBut** ligand is still coordinated to Ln^{3+} to maintain the neutral charge and at least one chromophore Bphen molecule remains coordinated to the metal. Hence excitation at the ligand absorption wavelength induces characteristic Ln^{3+} emission. In addition, residual ligand emission was observed in the **S-Tb-a** and **S-Tb-b** spectra, pointing to back transfer energy from the Tb^{3+} emitting level to the triplet state of the ligand or a possible equilibrium between the free ligand and the lanthanide complex. ^1H-NMR spectra of **S-Eu-a** and **S-Tb-b** derivatives in deuterated DCM solutions show a dynamic equilibrium between species of different geometries with possibly an exchange of the Bphen ligand between a bound and a free form. In contrast, the chiral carboxylic acid appears mostly bonded to the Ln in both cases. There is no evidence of a trend of red or blue shifting of the emission bands in the solid state with respect to the DCM solution ones, Fig. S7.†

Photoluminescence quantum yield (ϕ^L_{Ln}) and luminescence decay time (τ_{obs})

The overall photoluminescence quantum yields (ϕ^L_{Ln}) and luminescence lifetimes (τ_{obs}) were measured for both polycrystalline and solution samples at room temperature, for compounds presenting higher emission intensity: **S-Eu-a**, **S-Tb-a** and **S-Tb-b** samples. The results are compiled in Table 1.

S-Eu-a is the compound showing the highest ϕ^L_{Ln} value which is about 2-fold greater in the polycrystalline sample (0.71) compared to the DCM solution (0.31). Also, **S-Eu-a** shows the longest τ_{obs} value among the presented compounds (1.90 ms). As for **S-Tb-a** and **S-Tb-b** complexes, **S-Tb-a** showed higher luminescence intensity when comparing the emission spectra of the polycrystalline samples. This trend was also followed in the measured ϕ^L_{Ln} values where the **S-Tb-b** quantum yield was reduced by half (0.5) compared to that in **S-Tb-a** (0.10). Meanwhile for the 1 mM DCM Tb^{3+} samples, the measured ϕ^L_{Ln} value turned out to be the same for both **S-Tb-a** and **S-Tb-b** (0.015), suggesting once more that the mentioned Ln^{3+} compounds go through a structural change due to solvating effects and when the Tb polycrystalline complexes, whether *structure a* or *structure b*, dissolve the final arrangement found in the solution is the same. In addition, the $\tau_{obs\ polycryst}$ value of **S-Tb-a** is slightly greater than that of **S-Tb-b**, being 0.40 for

Table 1 Overall quantum yields and luminescence lifetime of compounds **S-Eu-a**, **S-Tb-a** and **S-Tb-b** measured in polycrystalline samples ($\phi^L_{Ln\ polycryst}$ and $\tau_{obs\ polycryst}$) and DCM solutions ($\phi^L_{Ln\ DCM}$ and $\tau_{obs\ DCM}$). The samples were excited at the respective absorption maxima (see Luminescence properties section of the Experimental section)

	$\phi^L_{Ln\ polycryst}$	$\phi^L_{Ln\ solution}$	$\tau_{obs\ polycryst}$ (ms)	$\tau_{obs\ solution}$ (ms)
S-Eu-a	0.71	0.31	1.90	1.80
S-Tb-a	0.10	0.015	0.40	[a]
S-Tb-b	0.05	0.015	0.30	[a]

[a] Value not recorded due to limitations in the equipment.
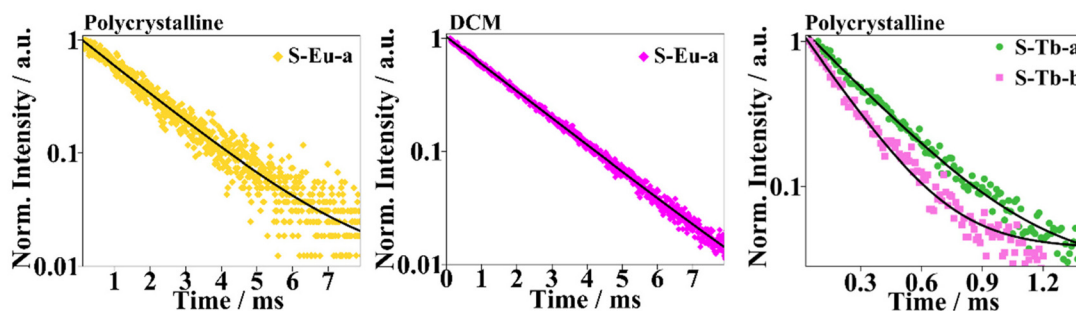
Fig. 4 Lifetime curves of compounds **S-Eu-a**, **S-Tb-a** and **S-Tb-b**. Solid lines represent mono-exponential fittings.

structure a and 0.30 for *structure b*. All decay curves could be fitted by a monoexponential decay law, Fig. 4. The presence of a single decay time component, τ_{obs}, for the former compounds is suggestive of a single radiative deactivation process, both in the solid state and in solution.

More information concerning the sensitization mechanism of **S-Eu-a** can be extracted from the spectroscopic data. The radiative lifetime (τ_{rad}) is consistent with the luminescence lifetime in the absence of non-radiative deactivation and it is different for each compound, since it depends on the Eu^{3+} environment and on the refractive index of the medium in which the emitting sample is found. The τ_{rad} value from the $^5D_0$ emissive state can be calculated from the corrected emission spectrum of **S-Eu-a** by means of a simplified equation (eqn (S1)†).[26,27] For the **S-Eu-a** polycrystalline sample, the τ_{rad} values are 2.29 ms and 3.40 ms for the DCM solution. Then the intrinsic quantum yields (ϕ_{Ln}^{Ln}) are 0.82 and 0.52 for the solid and solution samples respectively (see section 3 of the ESI†). Moreover, the sensitization efficiency (η_{sens}) describes the energy transferred from the absorbing ligands to the Ln^{3+} and it assumes a significant role in the overall quantum yield defined as $\phi_{Ln}^{L} = \eta_{sens} \cdot \phi_{Ln}^{Ln}$. Hence, the η_{sens} values of 0.86 in polycrystalline powder and 0.60 in DCM solution demonstrate a rather efficient sensitization effect from the ligand moieties to the Eu^{3+} emitting energy level, particularly when **S-Eu-a** is found as a polycrystalline sample. Moreover, if the dinuclear Eu^{3+} coordination compound **S-Eu-a** remains after dissolving it in 1 mM DCM solution, the relation $\tau_{rad\text{-}DCM} = \frac{n_{polycryst.}^3}{n_{DCM}^3} \tau_{rad\text{-}polycryst.}$ should be obeyed and $\tau_{rad\text{-}DCM}$ will yield 2.80 ms. However, the calculated $\tau_{rad\text{-}DCM}$ from the corrected emission spectra is 3.4 ms. The former fact suggests that the system found in solution differs from the one in the polycrystalline sample.[27]

Circular dichroism (CD) and circular polarized luminescence (CPL) measurements

Circular Dichroism (CD) measurements were carried out in the solid state preparing each polycrystalline sample dispersed into a KBr matrix. The CD spectra of powder samples turned out to be very weak and it was not possible to derive a significant interpretation. Mirror images could be discerned only for the **S/R-Tb-b** enantiomeric pair in the 210–400 nm range assigned to ligand absorption, Fig. S8.† Nevertheless, the spectrum shows rather weak cotton effects. For the presented dinuclear complexes, Bphen ligands coordinated to the lanthanide ion are quasi-coplanar in the crystal lattice, defining an overall low dissymmetry to the final compound, therefore leading to the absence of significant exciton coupling. In addition, the CD spectra were measured in 1 mM DCM solution. As already seen in the luminescence studies, the dinuclear lanthanide entities undergo a structural change, perhaps forming a mononuclear arrangement with both the enantiopure *R/S*-2-PhBut and Bphen ligands, coordinated to the lanthanide ion. The new species formed in DCM solution acquire higher dissymmetry, hence stronger CD spectra are obtained (Fig. 5 and Fig. S9†). Mirror image spectra are obtained for the enantiomeric pairs in the Bphen absorption wavelength, indicating that the chirality of the *R/S*-2-PhBut ligand is transferred to the chromophore Bphen. The band found at 300 nm in the CD spectra of Tb^{3+} and Dy^{3+} complexes is not found for the Eu^{3+} analogues, Fig. S8.†

Circular Polarized Luminescence (CPL) spectra were recorded in the solid state and 1 mM DCM for compounds showing the highest luminescence emission intensity: **R/S-Eu-a**, **R/S-Tb-a** and **R/S-Tb-b** enantiomeric pairs at the excitation wavelength of 365 nm in the solid state and 254 nm for the 1 mM DCM solution.

The solid samples were dispersed in a quartz plate, from a suspension in *n*-pentane, considering that the compounds are not soluble in this solvent. Solid deposition of compounds **R/S-Eu-a** shows rather weak but measurable mirror image signals for the $^5D_0 \rightarrow {}^7F_1$ and $^5D_0 \rightarrow {}^7F_2$ transitions (Fig. S10†). Due to the weak and noisy spectra obtained for the **R/S-Eu-a** polycrystalline pair, the reliably dissymmetry factor, g_{lum}, could not be extracted. Moreover, **R/S-Tb-b** exhibited only the most intense emission band corresponding to the $^5D_4 \rightarrow {}^7F_5$ transition. For this transition, three components with opposite signs (+, −, + for the *S*-enantiomer) can be distinguished (Fig. 6 and Fig. S11†) and the dissymmetry factor was $g_{lum} = \pm 2 \times 10^{-3}$ (+ for **S-Tb-b**), Table 2. Meaningful CPL spectra could not be obtained for compound **R/S-Tb-a**.
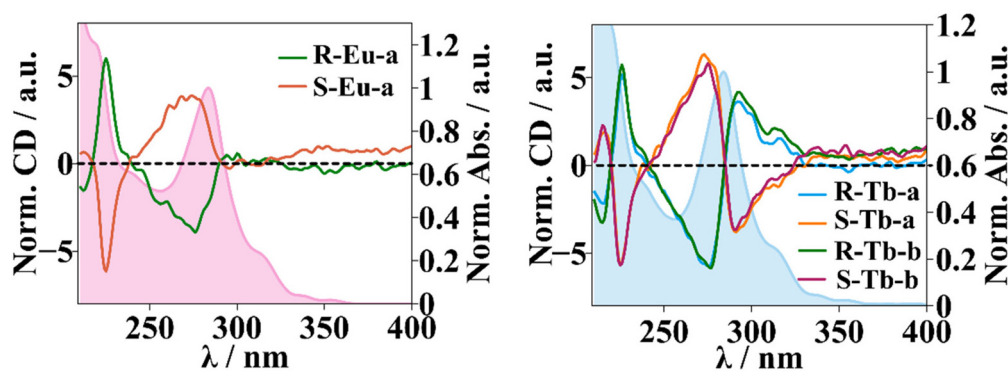
Fig. 5 Circular dichroism spectra of compounds *R/S*-Eu-a, *R/S*-Tb-a and *R/S*-Tb-b measured in 1 mM DCM solution.
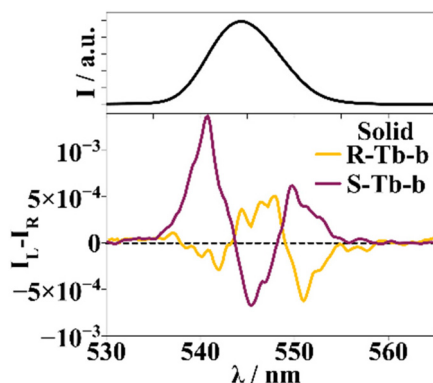

Fig. 6 Top: *R/S*-Tb-b emission of the $^5D_4 \rightarrow {}^7F_5$ transition. Bottom: solid state CPL spectra of *R/S*-Tb-b complexes on a quartz plate deposition.

Table 2 g_{lum} values of the *R/S*-Tb-a and *R/S*-Tb-b enantiomeric pair measured for the polycrystalline sample and in 1 mM DCM solution

g_{lum}	$^5D_4 \rightarrow {}^7F_5$
R/S-Tb-b polycrystalline	$\pm 2 \times 10^{-3}$ (+ for *S*-Tb-b)
R/S-Tb-a 1 mM DCM	± 0.03 (− for *S*-Tb-a)
R/S-Tb-b 1 mM DCM	± 0.03 (− for *S*-Tb-b)

The CPL spectra of Eu^{3+} and Tb^{3+} 1 mM DCM solutions were measured and under such conditions, the spectra significantly differ from the ones measured in powder depositions. Following the same trend as for CD, the CPL measurements of *S/R*-Eu-a, *S/R*-Tb-a and *S/R*-Tb-b DCM solutions were more intense and clearer. Well resolved mirror images were obtained for the *S/R*-Eu-a enantiomeric pair, as shown in Fig. 7a. The most intense band, as generally seen in the CPL of chiral Eu^{3+} compounds, is due to the pure magnetic dipole $^5D_0 \rightarrow {}^7F_1$ transition. It is split into two components with opposite signs (+, − for the *R*-enantiomer) corresponding to the $m_j = \pm 1$ and 0 states generated by crystal field perturbation. The g_{lum} factors obtained for the *R/S*-Eu-a pair range from ± 0.03 (+ for *R*-Eu-a) for the most intense component of $^5D_0 \rightarrow {}^7F_1$ to $\pm 8 \times 10^{-4}$ (+

for *R*-Eu-a) for the electric dipole $^5D_0 \rightarrow {}^7F_2$ transition, Fig. S12† and Table 3.

The DCM solutions of Tb-based systems also presented well resolved CPL (Fig. 7b). *R/S*-Tb-b shows mirror image spectra where the band arising from the $^5D_4 \rightarrow {}^7F_5$ transition clearly stands out among the others. It presents three components, each with alternating different signs (−, +, − for the *S*-enantiomer). Interestingly the sign of the crystal field components of this band is the opposite in the solid state *S/R*-Tb-b pair CPL measurement. The g_{lum} value for the most intense component of the $^5D_4 \rightarrow {}^7F_5$ transition is ± 0.03 (− for the *S*-enantiomer), as presented in Fig. S13† and Table 3. The DCM solution of *R/S*-Tb-a showed the same CPL properties evidencing that the species obtained in the solution are the same for both compounds regardless of the structure in the crystal phase (*structure a* or *structure b*, Fig. 7 bottom). Similar CPL properties are found for other reported Eu^{3+} and Tb^{3+} polynuclear compounds measured in the solid state and in solution.[28–31]

Magnetic properties

Direct current (DC) magnetic susceptibility studies. Direct current magnetic susceptibility (χ_M) and magnetization (*M*) experiments were carried out primarily for the *R*-enantiomers on the polycrystalline samples, as *S*- and *R*-enantiomers are expected to exhibit identical magnetic properties. The χ_M measurements were carried out under an external direct current (dc) magnetic field of 0.3 T in the 2–300 K temperature range. The $\chi_M T$ dependence with *T* plots are presented in Fig. 8(a) and (b). At room temperature (300 K) the $\chi_M T$ values are 3.08, 2.18, 2.78, 23.17, 23.34, 28.48, 28.24, 14.45 and 4.78 cm^3 mol^{-1} K for *R*-Nd-a, *R*-Sm-a, *R*-Eu-a, *R*-Tb-a, *R*-Tb-b, *R*-Dy-a, *R*-Dy-b, *R*-Tm-b and *R*-Yb-b respectively. For two isolated Ln^{3+} cations, the calculated $\chi_M T$ values are: 3.28 cm^3 mol^{-1} K for the Nd^{3+} ground state $^4I_{9/2}$ and $g_J = 8/11$; 0.18 cm^3 mol^{-1} K for the Sm^{3+} ground state $^6H_{5/2}$ and $g_j = 2/7$; 0 cm^3 mol^{-1} K for the Eu^{3+} ground state $^7F_0$; 23.64 cm^3 mol^{-1} K for the Tb^{3+} ground state $^7F_6$ and $g_j = 3/2$; 28.34 cm^3 mol^{-1} K for the Dy^{3+} ground state $^6H_{15/2}$ and $g_J = 4/3$; 7.15 cm^3 mol^{-1} K for the Tm^{3+} ground state $^3H_6$ and $g_J = 7/6$; and 5.14 cm^3 mol^{-1} K for the Yb^{3+} ground state $^2F_{7/2}$ and $g_J = 8.7$.[3a]
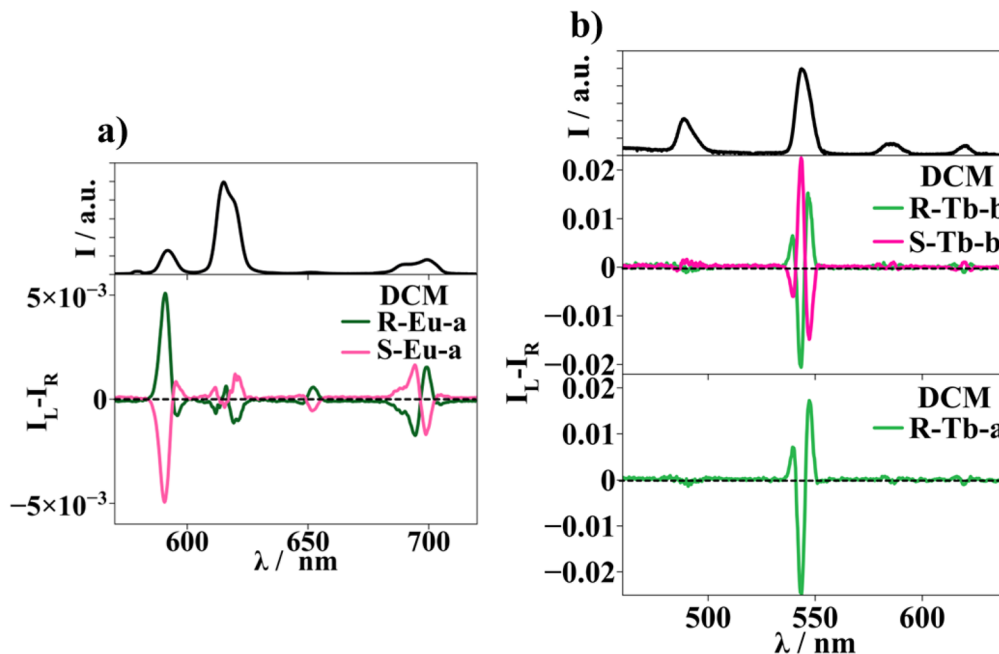
Fig. 7 CPL of 1 mM DCM solutions of compounds (a) *R/S*-Eu-a and (b) *R/S*-Tb-b and *R*-Tb-a. The black line in both figures represents the emission spectra of each luminescent compound.

Table 3 g_{lum} values of the *R/S*-Eu-a enantiomeric pair measured in 1 mM DCM solution

R/S-Eu-a 1 mM DCM	$^5D_0 \rightarrow {}^7F_1$	$^5D_0 \rightarrow {}^7F_2$	$^5D_0 \rightarrow {}^7F_3$
g_{lum}	±0.03 (+ for *R*-Eu-a)	±8 × 10⁻⁴ (+ for *R*-Eu-a)	±0.02 (+ for *R*-Eu-a)

The experimental $\chi_M T$ values at room temperature obtained for *R*-Sm-a and *R*-Eu-a are noticeably larger than the calculated ones, Fig. 8(a). The electronic ground states ^6H of a Sm³⁺ ion and ^7F of an Eu³⁺ ion split due to the spin–orbit coupling with $^6H_{J=5/2–15/2}$ and $^7F_{J=0–6}$ J states, respectively. For these ions the spin orbit coupling parameter (λ) is rather small, around

200 cm⁻¹ for Sm³⁺ and 300 cm⁻¹ for the Eu³⁺ ion. Due to the small λ values, excited J states are closer in energy, and these are found to be thermally populated at room temperature. Thus, the $\chi_M T$ value at 300 K is higher than the calculated one which only considers the population of the $^6H_{5/2}$ and $^5D_0$ ground states (for Sm³⁺ and Eu³⁺ respectively). The decrease of the $\chi_M T$ values on cooling the sample is due to the thermal depopulation of the excited J states. At 2 K, the $\chi_M T$ value of *R*-Eu-a is 0.01 cm³ mol⁻¹ K confirming that at low temperature the non-magnetic ground state ($J = 0$) is populated.[32]

The $\chi_M T$ *vs.* T curves of compounds *R*-Nd-a, *R*-Yb-b, *R*-Tb-a, *R*-Tb-b, *R*-Dy-a, *R*-Dy-b and *R*-Tm-a decrease on cooling the samples down to 1.12, 2.69, 15.69, 11.34, 19.34, 21.39, and 12.13 cm³ mol⁻¹ K at 2 K, respectively. Fig. 8(a) and (b). The decrease of $\chi_M T$ is attributed to the thermal depopulation of
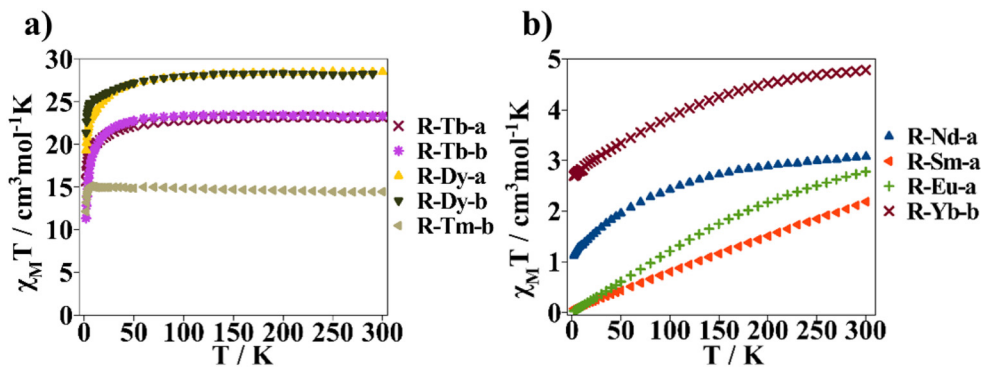

Fig. 8 (a) $\chi_M T$ *vs.* T plot, measured under an external magnetic dc field of 0.3 T, of compounds *R*-Tb-a, *R*-Tb-b, *R*-Dy-a, *R*-Dy-b and *R*-Tm-b and (b) *R*-Nd-a, *R*-Sm-a, *R*-Eu-a and *R*-Yb-b.

the excited $\pm m_j$ states of the ground J state. At the lowest temperature limit, **R-Tb-b** drops to smaller $\chi_M T$ values compared to **R-Tb-**a while **R-Dy-a** decreases more compared to **R-Dy-b**. The decrease of $\chi_M T(T)$, on cooling the sample, could be attributed to one phenomenon or a combination of different phenomena: first, due to the thermal depopulation of the excited m_j doublets, from the ground J state; second, due to weak antiferromagnetic coupling between the Ln^{3+} centers though the contracted nature of 4f electrons in lanthanide(III) ions making magnetic exchange coupling interactions rather weak; and third, due to dipolar interactions between the molecules of the crystal lattice.[3a,32a,33]

Magnetization dependence with applied magnetic field curves monitored at 2 K for the former compounds are depicted in Fig. S14.† Magnetization increases suddenly on applying an external magnetic field from 0 to ~1 T. The compounds do not show saturation of magnetization while the magnetization of **R-Eu-a** is maintained at 0 $N\mu_B$, as expected.[34b]

Alternating current (AC) magnetic susceptibility studies. Furthermore, alternating current (AC) magnetic susceptibility measurements, under an oscillating 4×10^{-4} T magnetic field, were carried out for compounds **R-Nd-a**, **R-Sm-a**, **R-Tb-a**, **R-Tb-b**, **R-Dy-a**, **R-Dy-b**, **R-Tm-b** and **R-Yb-b**. The samples containing Dy^{3+}, Nd^{3+} and Yb^{3+} showed slow relaxation of the magnetization.

Concerning Dy-based compounds, the magnetic behavior is quite different when varying from *structure a* (**R-Dy-a**) to *structure b* (**R-Dy-b**). At a 0 T direct current (H_{dc}) magnetic field, the

AC response of **R-Dy-a** was absent, while **R-Dy-b** showed maxima of the out-of-phase magnetic susceptibility component (χ''_M) and therefore Single Molecule Magnet (SMM) behavior, as shown in Fig. S15.† However, compound **R-Dy-a** showed a slow relaxation of magnetization at an H_{dc} value of just under 0.1 T; at $H_{dc} = 0$ T, **R-Dy-b** shows maxima in the χ''_M *vs.* ν curves above 6.5 K, Fig. 9a. The Cole–Cole plot (χ'_M *vs.* χ''_M), Fig. 9b, shows non-symmetric semicircles that can be fitted with the one component generalized Debye model described by the Casimir–Dupré function eqn (S3).†[35] The fitting leads to α values that remain almost constant along all the temperature range: 0.27 (1.8 K)–0.28 (6.5 K). The extracted relaxation times with temperature ($\ln(\tau)$ *vs.* $1/T$) are depicted in Fig. 9c. Interestingly, in the $\ln(\tau)$ *vs.* T^{-1} curve no clear linear trend is discerned in the high temperature range suggesting that the spin relaxation of **R-Dy-b** does not take place through the thermally activated, over-barrier Orbach mechanism described with eqn (2).[36]

$$\tau^{-1} = \tau_0^{-1} \exp\left(\frac{-\Delta E}{k_B T}\right) \quad (2)$$

From the fit with eqn (2) in the higher temperature range of the **R-Dy-b** curve, an activation energy of 2.85 cm^{-1} was obtained; therefore, we could propose the idea that the Orbach mechanism is not prevailing.[37] Nonetheless, it could be possible that for **R-Dy-b**, the magnetization relaxation takes place in the low energy vibrational structure (by low energy acoustic phonons) through the Raman mechanism as already experi-
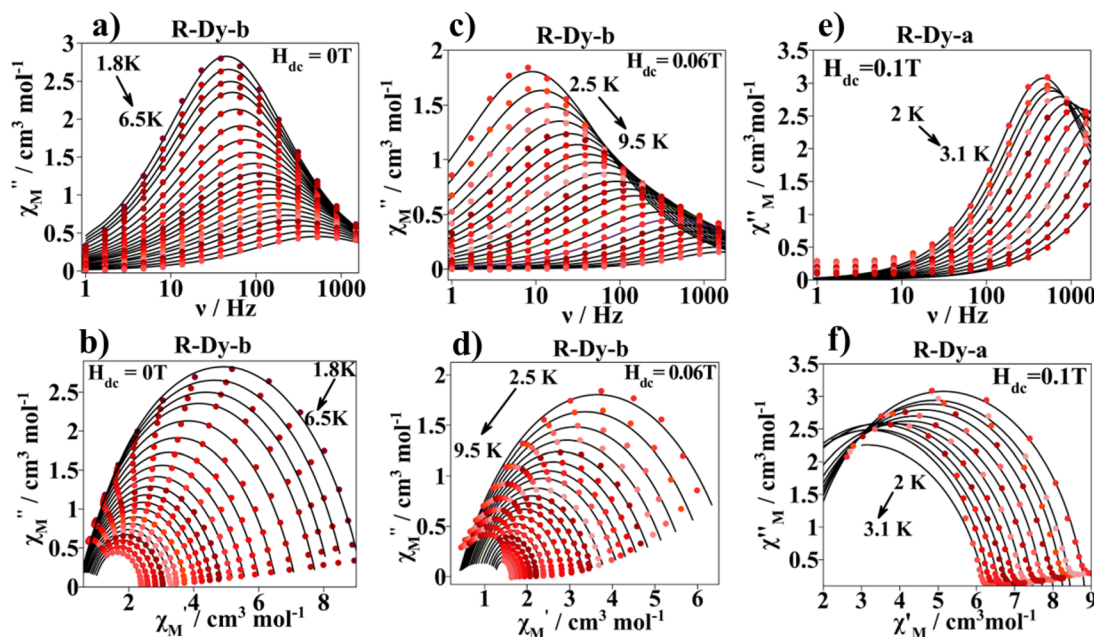
Fig. 9 (a) χ''_M *vs.* frequency plot obtained at $H_{dc} = 0$ T for **R-Dy-b**. (b) The Cole–Cole plot for **R-Dy-b** from the ac data recorded at $H_{dc} = 0$ T. The continuous black line corresponds to the best fit according to eqn (S3).† (c) The χ''_M *vs.* frequency plot obtained at $H_{dc} = 0.06$ T for **R-Dy-b**. (d) The Cole–Cole plot for **R-Dy-b** from the ac data recorded at $H_{dc} = 0.06$ T. The continuous black line corresponds to the best fit according to eqn (S3).† (e) The χ''_M *vs.* frequency plot obtained at $H_{dc} = 0.1$ T for **R-Dy-a**. (f) The Cole–Cole plot for **R-Dy-a** from the ac data recorded at $H_{dc} = 0.1$ T. The continuous black line corresponds to the best fit according to eqn (S3).†

enced in other Dy-based systems showing slow relaxation of the magnetization.[38,34c]

$$\tau^{-1} = CT^n + \tau_{\text{QTM}}^{-1} \tag{3}$$

The best fit of the **R-Dy-b** $\ln(\tau)$ *vs.* T^{-1} curve is obtained when Raman and quantum tunneling of magnetization (QTM) mechanisms (eqn (3)) are considered, and the obtained parameters are $C = 28.6 \text{ s}^{-1} \text{ K}^{-n}$ with $n = 2.4$ for Raman and $\tau_{\text{QTM}} = 0.0097$ s for QTM processes, as shown in Fig. 10. A compilation of the fitted parameters from the equations of the presented compounds is found in Table 4.

The χ''_{M} field dependence of **S-Dy-b** measured at 3.5 K shows that relaxation of the magnetization times ($\tau = 1/2\pi\nu$) reach the highest value at the optimal field of 0.06 T, as shown in Fig. S16.† At $H_{\text{dc}} = 0.06$ T, $\chi''_{\text{M}}(\nu)$ maxima appear at lower frequencies and at a higher temperature range (2.5–9 K) compared to that obtained from the $H_{\text{dc}} = 0$ T measurement, Fig. 9(c). The χ''_{M} peaks move progressively to higher oscillating frequencies on increasing the temperature suggesting that the spin relaxation of **S-Dy-b**, at $H_{\text{dc}} = 0.06$ T, takes place through a thermal dependent mechanism. The Cole–Cole plots were fitted with eqn (S3)† and Fig. 9(d). The α parameter remains near 0 throughout the temperature range: 0.011 (2.5 K)–0.014 (9 K), indicating that the width distribution of the relaxation times diminishes on applying $H_{\text{dc}} \neq 0$ T for the
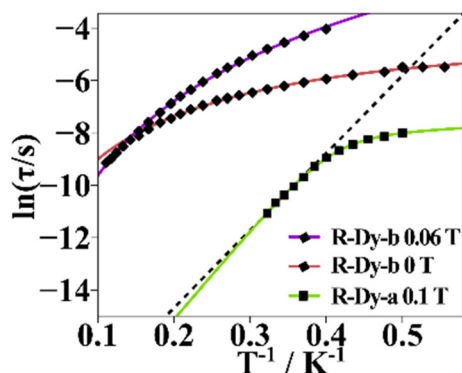
Fig. 10 The $\ln(\tau)$ *vs.* $1/T$ plot of **R-Dy-b** obtained at $H_{\text{dc}} = 0$ T, that for **R-Dy-b** obtained at $H_{\text{dc}} = 0.06$ T and that for **R-Dy-a** obtained at $H_{\text{dc}} = 0.1$ T. Continuous lines represent the best fit according to Raman + QTM equations for **R-Dy-b** at $H_{\text{dc}} = 0$ T, the Raman plot for **R-Dy-b** at $H_{\text{dc}} = 0.06$ T and Orbach + direct equations for **R-Dy-a** at $H_{\text{dc}} = 0.1$ T.

SMM Dy^{3+} compound. As the $\ln(\tau)$ *vs* T^{-1} plot shows, a lack of a clear linear trend in the higher temperature range is also identified for this experiment, as shown in Fig. 10. The best fit of the curve is obtained when only the equation corresponding to the Raman relaxation mechanism (first term of eqn (3)) is considered and the obtained parameters are $C = 1.2 \text{ s}^{-1} \text{ K}^{-n}$ with $n = 4$. The fast QTM is removed by applying an external magnetic field.

For **S-Dy-a**, magnetic field-dependent -measurements at 2 K show that τ is the greatest when the H_{dc} is 0.1 T, as shown in Fig. S17.† Therefore, χ'_{M} and χ''_{M} measurements were monitored at an H_{dc} value of 0.1 T. **R-Dy-a** showed maxima of the χ''_{M} component in a small temperature range (2–3.1 K), Fig. 9(e). Cole–Cole plots, presented in Fig. 9(f), show non-symmetric semicircles that become incomplete on increasing the temperature. They were successfully fitted with eqn (S3),† leading to α values in the range of 0.008 (2 K)–0.2 (at 3.1 K). The $\ln(\tau)$ *vs.* T^{-1} plot shows that at a higher temperature range, few points follow a linear trend, as shown in Fig. 10. The $\ln(\tau)$ *vs.* T^{-1} curve of **S-Dy-a** was fitted considering only the Orbach mechanism in the higher temperature range thus leading to an effective energy barrier of 18.89 cm^{-1} (27.19 K) and a pre-exponential factor (τ_0) of 2.59×10^{-9} s. However, the linear trend is not followed in the entire temperature range. The equations that fit best the magnetic data of **S-Dy-a** are the ones that describe the Orbach (followed in the high temperature range) and Direct (appears on cooling the sample) mechanisms. The best values of the fitting are $\Delta E = 23.5 \text{ cm}^{-1}$ (33.7 K) and τ_0 of 3.2×10^{-10} s for Orbach and $A = 1425.0 \text{ s}^{-1}$ K^{-1} for Direct. Although the ΔE of **S-Dy-a** is larger compared to the value calculated for **S-Dy-b**, it is still quite low. To verify if the **S-Dy-b** magnetization is relaxing through the Orbach mechanism, *ab initio* calculations should be performed to determine the energy difference between $\pm m_j$ ground and excited states. With such a low energy barrier, the Raman relaxation could be prevailing in the magnetization relaxation although, in this case, no successful fit could be obtained using the equation describing such a mechanism. Nevertheless, the temperature range in which **S-Dy-a** shows the AC response is very small (there is a 1 K temperature difference); therefore it is difficult to interpret the τ tendency with temperature since quite empirical data are obtained.

At $H_{\text{dc}} = 0$ T, compounds **R-Nd-a** and **R-Yb-b** do not show a χ''_{M} response under the ac magnetic field indicating that the

Table 4 Compilation of the fitted parameters of the equations that describe the best relaxation of the magnetization mechanism of compounds presenting slow relaxation of the magnetization

	Orbach		Raman		Direct	QTM
	$\Delta E/\text{cm}^{-1}$ (K)	τ_0/s	$C/\text{s}^{-1} \text{ K}^{-n}$	n	$A/\text{s}^{-1} \text{ K}^{-1}$	τ_{QTM}
R-Nd-a			0.8	6.4	435.9	
R-Dy-a	23.5 (33.7)	3.2×10^{-10}			1425.0	
R-Dy-b $H_{\text{dc}} = 0$ G			28.6	2.4		0.0097
R-Dy-b $H_{\text{dc}} = 500$ G			1.2	4.1		
R-Yb-b			1.26	5.7	126.5	
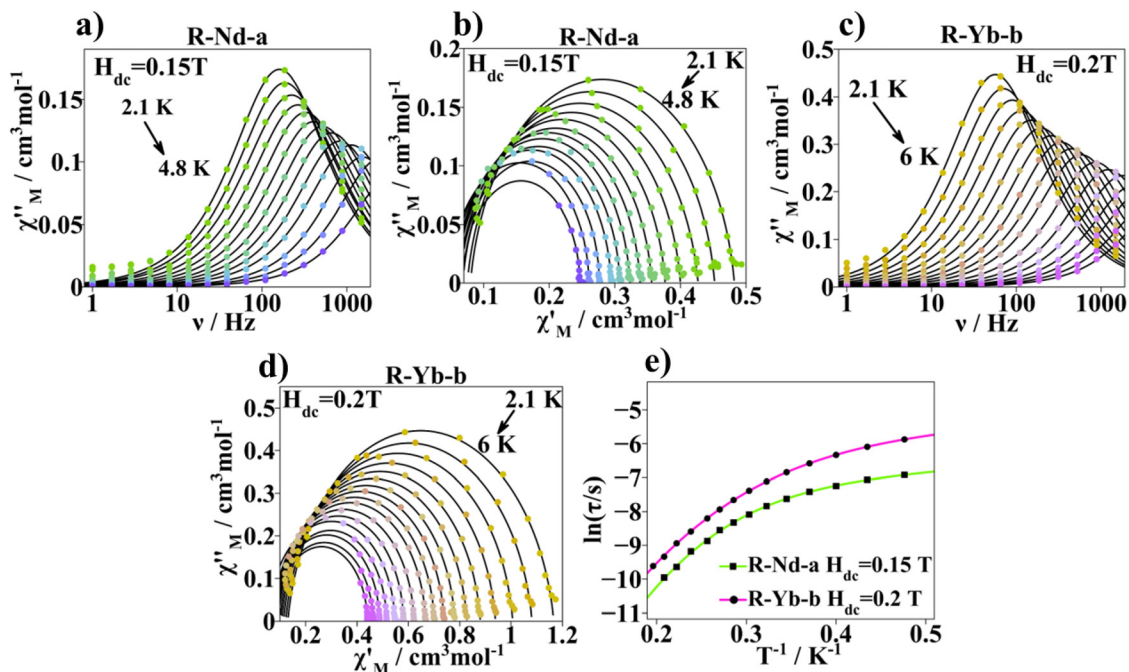
Fig. 11 (a) The χ''_M vs. frequency plot obtained at H_{dc} = 0.15 T for **R-Nd-a**. (b) The Cole–Cole plot for **R-Nd-a** obtained from the ac data recorded at H_{dc} = 0.15 T. The continuous black line corresponds to the best fit according to eqn (S3).† (c) The χ''_M vs. frequency plot obtained at H_{dc} = 0.2 T for **R-Yb-b**. (d) The Cole–Cole plot for **R-Yb-b** obtained from the ac data recorded at H_{dc} = 0.2 T. The continuous black line corresponds to the best fit according to eqn (S3).† (e) The $\ln(\tau)$ vs. 1/T plot of **R-Nd-a** obtained at H_{dc} = 0.15 T and that for **R-Yb-b** obtained at H_{dc} = 0.2 T. Continuous lines represent the best fit according to Raman + direct equations for both compounds.

relaxation of the magnetization goes through a relaxation mechanism of a quantum nature, the so-called QTM. Field-dependent measurements were performed at constant temperatures of 2 and 2.5 K, showing the highest τ values at the optimal fields of 0.15 T and of 0.2 T for **R-Nd-a** and **R-Yb-b**, respectively, as shown in Fig. S15.† Then, AC measurements at the optimal DC fields were taken for each compound. **R-Nd-a** showed maxima of imaginary susceptibility in the 2.1–4.8 K temperature range while the ac signal appeared in a wider temperature range of 2.1–6 K for **R-Yb-b**, as shown in Fig. 11(a) and (d). The Cole–Cole plot representation shows semicircles that can be well fitted with eqn (S3).† The collected α parameters stay close to 0 for both compounds: 0.0035–0.0103 for **R-Nd-a** and 0.094–0.01 for **R-Yb-b**. Moreover, the $\ln(\tau)$ vs. T^{-1} plot successfully fits to the sum of both contributions, Raman and Direct mechanisms (eqn (4)), Fig. 11(e). The values of the parameters obtained from the fitting yielded C = 0.8 s^{-1} K^{-n} with n = 6.4 for Raman and A = 435.9 s^{-1} K^{-1} for Direct for **R-Nd-a** and C = 1.26 s^{-1} K^{-n} with n = 5.74 for Raman and A = 126.3 s^{-1} K^{-1} for Direct for **R-Yb-b**. Other Yb^{3+} and Nd^{3+} compounds with slow relaxation of the magnetization under an external DC field showed similar behavior.[34a,d,e,37,39]

$$\tau^{-1} = CT^n + AH^4T \tag{4}$$

Finally, **R-Sm-a**, **R-Tb-a**, **R-Tb-b**, **R-Tm-b** samples do not show χ''_M dependence with either temperature or frequency under the oscillating magnetic field.

Conclusions

In the presented work, nine enantiomerically pure pairs have been successfully isolated. The new compounds consist of chiral dinuclear coordination complexes with the formula $[\text{Ln}_2(\mu\text{-}R/S\text{-}2\text{-PhBut})_4(R/S\text{-}2\text{-PhBut})_2(\text{Bphen})_2]$ where R/S-2-PhBut is R/S-2-phenylbutirate, Bphen refers to 4,7-diphenyl-1,10-phenanthroline and Ln = Nd^{3+} (**R/S-Nd-a**), Sm^{3+} (**R/S-Sm-a**), Eu^{3+} (**R/S-Eu-a**), Tb^{3+} (**R/S-Tb-a** and **R/S-Tb-b**), Dy^{3+} (**R/S-Dy-a** and **R/S-Dy-b**), Tm^{3+} (**R/S-Tm-b**) and Yb^{3+} (**R/S-Yb-b**). Single crystal X-ray diffraction reveals that two different structural motifs (*structure a* and *structure b*) are obtained along the lanthanide series, and the isolation of one or the other structural motif depends on the ionic radius of the Ln^{3+}.

Moreover, luminescence studies were carried out in the solid state and in 1 mM DCM solution. Excitation at the ligand absorption wavelengths resulted in the expected luminescence from the lanthanides Eu^{3+}, Tb^{3+}, Nd^{3+} and Yb^{3+}, both in the solid state and in DCM solutions. Circular dichroism and circular polarized luminescence measurements reveal weak spectra for the solid state Eu and Tb samples, although for the DCM solutions a clearer mirror image and more intense spectra were obtained. Correlation of luminescence, CD, CPL and ^{1}H-NMR studies reveals that the dinuclear structure undergoes a deep structural change on dissolving each polycrystalline sample in 1 mM DCM solution.

Magnetic measurements revealed Single Molecular Magnet (SMM) behaviour for compound **R-Dy-b** while slow relaxation

of the magnetization under an external magnetic field was observed in **R-Dy-a**, **R-Nd-a** and **R-Yb-b**. Magnetization relaxation of **R-Dy-b**, **R-Nd-a** and **R-Yb-b** is described by the Raman mechanism. The dominance of the Raman rather than the Orbach relaxation may originate from a lack of axiality in the Ln^{3+} coordination sphere provided by the selected ligands.

Data availability

The data supporting this article have been included as part of the ESI.†

Crystallographic data for **S-Eu-a** and **S-Tm-b** have been deposited at the Cambridge Crystallographic Data Centre with CCDC numbers 2330935 and 2330936 respectively.

Conflicts of interest

There are no conflicts to declare.

Acknowledgements

References

1 N. Ishikawa, M. Sugita, T. Ishikawa, S. Y. Koshihara and Y. Kaizu, *J. Am. Chem. Soc.*, 2003, **125**, 8694–8695.

2 (*a*) J. Tang and P. Zhang, *Lanthanide Single Molecule Magnets*, Springer-Verlag, Berlin Heidelberg, 2015; (*b*) H. L. C. Feltham and S. Brooker, *Coord. Chem. Rev.*, 2014, **276**, 1–33; (*c*) D. N. Woodruff, R. E. P. Winpenny and R. A. Layfield, *Chem. Rev.*, 2013, **113**, 5110–5148; (*d*) A. Zabala-Lekuona, J. M. Seco and E. Colacio, *Coord. Chem. Rev.*, 2021, **441**, 213984; (*e*) A. Borah and R. Murugavel, *Coord. Chem. Rev.*, 2022, **453**, 214288.

3 (*a*) *The Rare Earth Elements, Fundamentals and Applications*, ed. D. A. Atwood, John Wiley& Sons Ltd, 2012; (*b*) Z. Xia, Z. Xu, M. Chen and Q. Liu, *Dalton Trans.*, 2016, **45**, 11214–11232; (*c*) J.-C. G. Bünzli and C. Piguet, *Chem. Soc. Rev.*, 2005, **34**, 1048–1077; (*d*) J.-C. G. Bünzli, *Acc. Chem. Res.*, 2006, **39**, 53–61; (*e*) S. Swavey and R. Swavey, *Coord. Chem. Rev.*, 2009, **253**, 2627–2638; (*f*) S. V. Eliseeva and J.-C. G. Bünzli, *Chem. Soc. Rev.*, 2010, **39**, 189–227; (*g*) E. G. Moore, A. P. S. Samuel and K. N. Raymond, *Acc. Chem. Res.*, 2009, **42**, 542–552; (*h*) C. P. Montgomery, B. S. Murray, E. J. New, R. Pal and D. Parker, *Acc. Chem. Res.*, 2009, **42**, 925–937; (*i*) S. J. Butler, M. Delbianco, L. Lamarque, B. K. McMahon, E. R. Neil, R. Pal, D. Parker, J. W. Walton and J. M. Zwier, *Dalton Trans.*, 2015, **44**, 4791–4803; (*j*) J. C. Bünzli, *Coord. Chem. Rev.*, 2015, **293–294**, 19–47; (*k*) Q. Zhang, W. Ge, X. Zhang and X. Chen, *Dalton Trans.*, 2022, **51**, 8714–8722; (*l*) P. Pradhan, S. Priya, M. Rajendran, K. Singh and S. Vaidyanathan, *Dalton Trans.*, 2022, **51**, 715–730.

4 (*a*) G. Koeckelberghs, S. Sioncke, T. Verbiest, A. Persoons and C. Samyn, *Chem. Mater.*, 2003, **15**, 2870–2872; (*b*) S. Dang, J.-H. Zhang, Z.-M. Sun and H.-J. Zhang, *Chem. Commun.*, 2012, **48**, 11139–11141; (*c*) E. Peeters, M. P. T. Christiaans, R. A. J. Janssen, H. F. M. Schoo, H. P. J. M. Dekkers and E. W. Meijer, *J. Am. Chem. Soc.*, 1997, **119**, 9909–9910; (*d*) J. P. Leonard, P. Jensen, T. McCabe, J. E. O'Brien, R. D. Peacock, P. E. Kruger and T. Gunnlaugsson, *J. Am. Chem. Soc.*, 2007, **129**, 10986–10987; (*e*) F. Stomeo, C. Lincheneau, J. P. Leonard, J. E. O'Brien, R. D. Peacock, C. P. McCoy and T. Gunnlaugsson, *J. Am. Chem. Soc.*, 2009, **131**, 9636–9637.

5 (*a*) F. Zinna, U. Giovanella and L. Di Bari, *Adv. Mater.*, 2015, **27**, 1791–1795; (*b*) F. Zinna, M. Pasini, F. Galeotti, C. Botta, L. Di Bari and U. Giovanella, *Adv. Funct. Mater.*, 2017, **27**, 1603719; (*c*) F. Zinna, L. Arrico, T. Funaioli, L. di Bari, M. Pasini, C. Botta and U. Giovanella, *J. Mater. Chem. C*, 2022, **10**, 463–468.

6 (*a*) S. Shuvaev, E. A. Suturina, K. Mason and D. Parker, *Chem. Sci.*, 2018, **9**, 2296–3003; (*b*) M. Leonzio, A. Melchior, G. Faura, M. Tolazzi, M. Bettinelli, F. Zinna, L. Arrico, L. Di Bari and F. Piccinelli, *New J. Chem.*, 2018, **42**, 7931–7939; (*c*) J. Yuasa, T. Ohno, H. Tsumatori, R. Shiba, H. Kamikubo, M. Kataoka, Y. Hasegawa and T. Kawai, *Chem. Commun.*, 2013, **49**, 4604–4606; (*d*) K. M. Ayers, N. D. Schley and G. Ung, *Inorg. Chem.*, 2020, **59**, 7657–7665; (*e*) J. Gong and X. Zang, *Coord. Chem. Rev.*, 2022, **453**, 214329; (*f*) N. F. M. Mukthar, N. D. Schley and G. Ung, *J. Am. Chem. Soc.*, 2022, **144**, 6148–6153; (*g*) P. Stachelek, L. MacKenzie, D. Parker and R. Pal, *Nat. Commun.*, 2022, **13**, 553; (*h*) A. T. Frawley, R. Pal and D. Parker, *Chem. Commun.*, 2016, **52**, 13349–13352.

7 (*a*) M. Górecki, L. Carpita, L. Arrico, F. Zinna and L. Di Bari, *Dalton Trans.*, 2018, **47**, 7166–7177; (*b*) L. E. MacKenzie and R. Pal, *Nat. Rev.*, 2021, **5**, 109–124.

8 (*a*) F. Gendron, S. Di pietro, L. Abad Galán, F. Riobé, V. Placide, L. Guy, F. Zinna, L. Di Bari, A. Bensalah-Ledoux, Y. Guyot, G. Pilet, F. Pointillard, B. Baguenard, S. Guy, O. Cador, O. Maury and B. Le Guennic, *Inorg. Chem. Front.*, 2021, **8**, 914–926; (*b*) B. Lefeuvre, C. A. Mattei, J. Flores Gonzalez, F. Gendron, V. Dorcet, F. Riobé, C. Lalli, B. Le Guennic, O. Cador, O. Maury, S. Guy, A. Bensalh-Ledoux, B. Baguenard and F. Pointillard, *Chem. – Eur. J.*, 2021, **27**, 7362–7366.

9 (*a*) C. Dee, F. Zinna, W. R. Kitzmann, G. Pescitelli, K. Heinze, L. D. Bari and M. Seitz, *Chem. Commun.*, 2019, **55**, 13078–13081; (*b*) J. R. Jiménez, B. Doistau, C. M. Cruz, C. Besnard, J. M. Cuerva, A. G. Campaña and C. Piguet, *J. Am. Chem. Soc.*, 2019, **141**(33), 13244–13252; (*c*) J. R. Jiménez, M. Poncet, S. Míguez-Lago, S. Grass, J. Lacour, C. Besnard and J. M. Cuerva, *Angew. Chem., Int. Ed.*, 2021, **133**, 10183–10190; (*d*) M. Poncet, A. Benchohra, J. R. Jiménez and C. Piguet, *ChemPhotoChem*, 2021, **5**(10),

880–892; (e) O. G. Willis, F. Zinna and L. D. Bari, *Angew. Chem., Int. Ed.*, 2023, **62**, e202302358; (f) E. M. Sánchez-Carnerero, A. R. Agarrabeitia, F. Moreno, B. L. Maroto, G. Muller, M. J. Ortiz and S. de la Moya, *Chem. – Eur. J.*, 2015, **21**, 13488–13500; (g) L. Arrico, L. Bari and F. Zinna, *Chem. – Eur. J.*, 2020, **27**, 2920–2934; (h) M. Cei, L. Di Bari and F. Zinna, *Chirality*, 2023, **35**, 192–210.

10 (a) F. Zinna and L. Di Bari, *Chirality*, 2015, **27**, 1–13; (b) J. L. Lunkley, D. Shirotani, K. Yamanari, S. Kaizaki and G. Muller, *Inorg. Chem.*, 2011, **50**, 12724–12732; (c) F. Zinna, C. Resta, S. Abbate, E. Castiglioni, G. Longhi, P. Mineo and L. Di Bari, *Chem. Commun.*, 2015, **51**, 11903–11906; (d) L. Llanos, P. Cancino, P. Mella, P. Fuentealba and D. Aravena, *Coord. Chem. Rev.*, 2024, **505**, 215675; (e) H.-Y. Wong, W.-S. Lo, K.-H. Yim and G.-L. Law, *Chem*, 2019, **5**, 3058–3095.

11 (a) M. Cantuel, G. Bernardinelli, G. Muller, J. P. Riehl and C. Piguet, *Inorg. Chem.*, 2004, **43**, 1840–1849; (b) F. Stomeo, C. Lincheneau, J. P. Leonard, J. E. Obrien, R. D. Peacock, C. P. McCoy and T. Gunnlaugsson, *J. Am. Chem. Soc.*, 2009, **31**, 9636–9637.

12 (a) O. Mamula, M. Lama, S. G. Telfer, A. Nakamura, R. Kuroda, H. Stoeckli-Evans and R. Scopelitti, *Angew. Chem.*, 2005, **117**, 2583–2587; (b) M. Lama, O. Mamula, G. S. Kottas, F. Rizzo, L. De Cola, A. Nakamura, R. Kuroda and H. Stoeckli-Evans, *Chem. – Eur. J.*, 2007, **13**, 7358–7373.

13 G. Bozoklu, C. Gateau, D. Imbert, J. Pecaut, K. Robeyns, Y. Filinchuk, F. Memon, G. Muller and M. Mazzanti, *J. Am. Chem. Soc.*, 2012, **134**, 8372–8375.

14 (a) B. Casanovas, F. Zinna, L. Di Bari, M. S. El Fallah, M. Font-Bardía and R. Vicente, *Dalton Trans.*, 2017, **46**, 6349–6357; (b) B. Casanovas, S. Speed, M. S. El Fallah, R. Vicente, M. Font-Bardía, F. Zinna and L. Di Bari, *Dalton Trans.*, 2019, **48**, 2059–2067.

15 (a) K. Miyata, Y. Konno, T. Nakanishi, A. Kobayashi, M. Kato, K. Fushimi and Y. Hasegawa, *Angew. Chem., Int. Ed.*, 2013, **52**, 6413–6416; (b) Y. Kuramochi, T. Nakagawa, T. Yokoo, J. Yuasa, T. Kawaia and Y. Hasegawa, *Dalton Trans.*, 2012, **41**, 6634–6640; (c) H. Xin, F.-Y. Li, M. Shi, Z.-Q. Bian and C.-H. Huang, *J. Am. Chem. Soc.*, 2003, **125**, 7166–7167; (d) A. P. Bassett, S. W. Magennis, P. B. Glover, D. J. Lewis, N. Spencer, S. Parsons, R. M. Williams, L. D. Cola and Z. Pikramenou, *J. Am. Chem. Soc.*, 2004, **126**, 9413–8424; (e) X.-P. Yang, R. A. Jones and S.-M. Huang, *Coord. Chem. Rev.*, 2014, **273**, 63–75; (f) M. Tropiano, N. L. Kilah, M. Morten, H. Rahman, J. J. Davis, P. D. Beer and S. Faulkner, *J. Am. Chem. Soc.*, 2011, **133**, 11847–11849; (g) J. D. Moore, R. L. Lord, G. A. Cisneros and M. J. Allen, *J. Am. Chem. Soc.*, 2012, **134**, 17372–17375; (h) B. Alpha, J.-M. Lehn and G. Mathis, *Angew. Chem., Int. Ed. Engl.*, 1987, **26**, 266–267; (i) C. Bazzicalupi, A. Bencini, A. Bianchi, C. Giorgi, V. Fusi, A. Masotti, B. Valtancoli, A. Roque and F. Pina, *Chem. Commun.*, 2000, 561–562.

16 A. Tubau, F. Zinna, L. Di Bari, M. Font-Bardía and R. Vicente, *Dalton Trans.*, 2023, **52**, 1122–1132.

17 F. Zinna, T. Bruhn, C. A. Guido, J. Ahrens, M. Bröring, L. Di Bari and G. Pescitelli, *Chem. – Eur. J.*, 2016, **22**, 16089–16098.

18 G. M. Sheldrick, *Acta Crystallogr., Sect. A: Fundam. Crystallogr.*, 2008, **64**, 112–122.

19 G. M. Sheldrick, *Acta Crystallogr., Sect. C: Cryst. Struct. Commun.*, 2015, **71**, 3–8.

20 R. A. Coxall, S. G. Harris, D. K. Henderson, S. Parsons, P. A. Tasker and R. E. P. Winpenny, *J. Chem. Soc., Dalton Trans.*, 2000, 2349–2356.

21 (a) M. Llunell, D. Casanova, J. Cirera, P. Alemany and S. Alvarez, *Shape Program., version 2*, Universitat de Barcelona, Barcelona, Spain, 2010; (b) P. Alemany, D. Casanova, S. Alvarez, C. Dryzun and D. Avnir, *Rev. Comput. Chem.*, 2017, **30**, 289–352.

22 J. A. Peters, K. Djanashvili, C. F. G. C. Geraldes and C. Platas-Iglesias, *Coord. Chem. Rev.*, 2020, **106**, 213146.

23 (a) A. M. Kaczmarek, K. V. Hecke and R. V. Deun, *Inorg. Chem.*, 2014, **53**, 9498–9508; (b) S. Chemingui, M. Ferhi, K. Horchani-Naifer and M. Férid, *J. Lumin.*, 2015, **166**, 82–87.

24 K. Binnemans, *Coord. Chem. Rev.*, 2015, **295**, 1–45.

25 *Luminescence of Lanthanide Ions in Coordination Compounds and Nanomaterials*, ed. A. de Bettencourt-Dias, John Wiley & Sons Ltd, 2014.

26 M. H. V. Werts, R. T. F. Jukes and J. W. Verhoeven, *Phys. Chem. Chem. Phys.*, 2002, **4**, 1542–1548.

27 A. Aebischer, F. Gumy and J.-C. G. Bünzli, *Phys. Chem. Chem. Phys.*, 2009, **11**, 1346–1353.

28 (a) B. Casanovas, F. Zinna, L. Di Bari, M. S. El Fallah, M. Font-Bardía and R. Vicente, *Dalton Trans.*, 2017, **46**, 6349–6357; (b) B. Casanovas, S. Speed, M. S. El Fallah, R. Vicente, M. Font-Bardía, F. Zinna and L. Di Bari, *Dalton Trans.*, 2019, **48**, 2059–2067; (c) A. Tubau, F. Zinna, L. Di Bari, M. Font-Bardía and R. Vicente, *Dalton Trans.*, 2023, **52**, 1122–1132.

29 C. A. Mattei, K. Dhbaibi, B. Lefeuvre, V. Dorcet, G. Argouarch, O. Cador, B. Le Guennic, O. Maury, C. Lalli, S. Guy, A. Bensalah-Ledoux, F. Riobé, B. Baguenard and F. Pointillart, *Chirality*, 2022, **34**, 34–47.

30 (a) H.-Y. Wong, W.-S. Lo, K.-H. Yim and G.-L. Law, *Chem*, 2019, **5**, 3058–3095; (b) X.-Z. Li, C.-B. Tian and Q.-F. Sun, *Chem. Rev.*, 2022, **122**, 6374–6458; (c) Y. Kitagawa, M. Tsurui and Y. Hasegawa, *ACS Omega*, 2020, **5**, 3786–3791.

31 S. Ruggieri, S. Mizzoni, C. Nardon, E. Cavalli, C. Sissa, M. Anselmi, P. Giorgio Cozzi, A. Gualandi, M. Sanadar, A. Melchior, F. Zinna, O. G. Willis, L. Di Bari and F. Piccinelli, *Inorg. Chem.*, 2023, **62**, 8812–8822.

32 (a) M. Andruh, E. Bakalbassis, O. Kahn, J. C. Trombe and P. Porcher, *Inorg. Chem.*, 1993, **32**, 1616–1622; (b) O. Kahn, *Molecular Magnetism*, VHC Publishers, Inc., USA, 1993.

33 (a) J. Tang, I. Hewitt, N. T. Madhu, G. Chastanet, W. Wernsdorfer, C. E. Anson, C. Benelli, R. Sessoli and A. K. Powell, *Angew. Chem., Int. Ed.*, 2006, **45**, 1729–1733; (b) P.-H. Lin, W.-B. Sun, M.-F. Yu, G.-M. Li, P.-F. Yan and M. Murugesu, *Chem. Commun.*, 2011, **47**, 10993–10995.

34 (a) J. Mayans, L. Tesi, M. Briganti, M. E. Boulon, M. Font-Bardía, A. Escuer and L. Sorace, *Inorg. Chem.*, 2021, **60**, 8692–8703; (b) E. Lucaccini, J. J. Baldoví, L. Chelazzi, A.-L. Barra, F. Grepioni, J.-P. Costes and L. Sorace, *Inorg. Chem.*, 2017, **56**, 4728–4738; (c) E. Rousset, M. Piccardo, M.-E. Boulon, R. W. Gable, A. Soncini, L. Sorace and C. Boskovic, *Chem. – Eur. J.*, 2018, **24**, 14768–14785; (d) S. K. Gupta, T. Rajeshkumar, G. Rajaraman and R. Murugavel, *Chem. Commun.*, 2016, **52**, 7168–7171; (e) Y.-C. Chen, X.-S. Huang, J.-L. Liu and M.-L. Tong, *Inorg. Chem.*, 2018, **57**, 11782–11787.

35 H. B. G. Casimir, D. Bijl and F. K. Du Pré, *Physica*, 1941, **8**(4), 449–460.

36 K. N. Shrivastava, *Phys. Status Solidi B*, 1983, **117**, 437–458.

37 (a) F. S. Santana, M. Perfetti, M. Briganti, F. Sacco, G. Poneti, E. Ravera, J. F. Soares and R. Sessoli, *Chem. Sci.*, 2022, **13**, 5860–5871; (b) S. Mondal and A. Lunghi, *J. Am. Chem. Soc.*, 2022, **144**, 22965–22975; (c) M. Briganti, F. Santanni, L. Tesi, F. Totti, R. Sessoli and A. Lunghi, *J. Am. Chem. Soc.*, 2021, **143**, 13633–13645.

38 J. Long, B. G. Shestakov, D. Liu, L. F. Chibotaru, Y. Guari, A. V. Cherkasov, G. K. Fukin, A. A. Trifonov and J. Larionova, *Chem. Commun.*, 2017, **53**, 4706–4709.

39 (a) F. Guégan, J. Jung, B. L. Guennic, F. Riobé, O. Maury, B. Gillon, J. F. Jacquot, Y. Guyot, C. Morell and D. Luneau, *Inorg. Chem. Front.*, 2019, **6**, 3152–3157; (b) K. S. Pedersen, J. Dreiser, H. Weihe, R. Sibille, H. V. Johannesen, M. A. Sørensen, B. E. Nielsen, M. Sigrist, H. Mutka, S. Rols, J. Bendix and S. Piligkos, *Inorg. Chem.*, 2015, **54**, 7600–7606; (c) D. Q. Wu, D. Shao, X. Q. Wei, F. X. Shen, L. Shi, Y. Q. Zhang and X. Y. Wang, *Dalton Trans.*, 2017, **46**, 12884–12892; (d) W. Zhao, H. Cui, X.-Y. Chen, G. Yi, L. Chen, A. Yuan and C. L. Luo, *Dalton Trans.*, 2019, **48**, 5621–5626.